THERMAL SIGNATURE REDUCTION THROUGH LIQUID NITROGEN AND

WATER INJECTION

A Thesis

by

JASON ANTONIO GUARNIERI

Submitted to the Office of Graduate Studies of
Texas A&M University
in partial fulfillment of the requirements for the degree of

MASTER OF SCIENCE

December 2004

Major Subject: Aerospace Engineering

THERMAL SIGNATURE REDUCTION THROUGH LIQUID NITROGEN AND

WATER INJECTION

A Thesis

by

JASON ANTONIO GUARNIERI

Submitted to Texas A&M University
in partial fulfillment of the requirements
for the degree of

MASTER OF SCIENCE

Approved as to style and content by:

Paul G. A. Cizmas
(Chair of Committee)

Leland Carlson
(Member)

Othon Rediniotis
(Member)

Steven Taliaferro
(Member)

Walter Haisler
(Head of Department)

December 2004

Major Subject: Aerospace Engineering

ABSTRACT

Thermal Signature Reduction through Liquid Nitrogen and Water Injection.

(December 2004)

Jason Antonio Guarnieri, B.S., Texas A&M University

Chair of Advisory Committee: Dr. Paul G. A. Cizmas

The protection of aircraft against shoulder fired heat seeking missiles is of growing concern in the aviation community. This thesis presents a simple method for shielding the infrared signature of a jet engine from heat seeking missiles. The research efforts investigated two approaches to shield the thermal signature of the Noel Penny Type 401 turbojet at the Texas A&M University Propulsion Lab Test Cell. First, liquid nitrogen was injected through a manifold at a flow rate equivalent to the flow rate of exhaust gases, producing a small temperature reduction in the exhaust but no infrared shielding. Second, water was injected at a flow rate of 13% of the flow of exhaust gases, producing a greater temperature reduction and some shielding. Water was then injected through a manifold at a flow rate of 118% of the flow rate of exhaust gases, producing a substantial reduction in temperature and complete shielding of the infrared signature. Additionally, numerical simulations were performed using FLUENT to support these experiments. Results are presented in the form of thermocouple data and thermal images from the experiments, and in the form of temperature contours and streamtraces from the simulations.

To my parents William and Nancy and to my fiancée Jennifer.

ACKNOWLEDGMENTS

First I would like to thank my advisor, Dr. Paul Cizmas, for his guidance throughout the project. Additionally, I would like to thank the members of my thesis committee, Dr. Leland Carlson, Dr. Othon Rediniotis, and Dr. Steven Taliaferro for their guidance and excellent classroom instruction. Special thanks to Dr. Dale Webb; without his involvment this project would not have been possible. I would also like to thank two of my fellow students Steven Chambers and Joaquin Gargoloff and my brother Stephen Guarnieri for their much needed assistance in the lab. Finally, I must thank my parents for their steadfast support and encouragement from the beginning, and most importantly, I am exceptionally grateful to my fiancé Jennifer, who endured time and distance for me.

NOMENCLATURE

Abbreviations		Definitions
AM	-	Amplitude modulation
CFD	-	Computational fluid dynamics
CM	-	Countermeasures
DAQ	-	Data acquisition
EM	-	Electromagnetic
EMR	-	Electromagnetic radiation
FM	-	Frequency modulated
FPA	-	Focal plane array
IR	-	Infrared
IRCCM	-	Infrared counter-countermeasures
LN_2	-	Liquid nitrogen
NPT	-	Noel Penny Turbines Limited
NPT401	-	NPT type 401 turbojet
TAMU	-	Texas A&M University
TCs	-	Thermocouples
UV	-	Ultraviolet

TABLE OF CONTENTS

LIST OF TABLES

LIST OF FIGURES

FIGURE   Page

CHAPTER I

INTRODUCTION

The first guided missile prototypes were built in the decade following World War II. Initially, these missiles used radar technology, which proved to be expensive and problematic. Around 1947, a Naval physicist named Bill McLean devised a way to avoid the problems associated with radar guided missiles. He began to develop a new system that could track the heat given off by the enemies' propulsion system. McLean's new *heat seeking* missile had two main advantages over the radar guided missiles then currently under development. First, heat seeking missiles use a small photovoltaic infrared (IR) sensor rather than bulky radar equipment, making them smaller, lighter and less expensive per unit. Second, heat seeking missiles track a target using the IR energy emitted by the engine(s) rather than receiving radio waves reflected off the target. Consequently, heat seeking missiles are *fire and forget*, giving the pilot the ability to fire his missile and then get himself and his aircraft clear of the danger zone.

To defend aircraft against this emerging missile threat, engineers began to develop countermeasures (CM). The most popular CM are pyrotechnic infrared decoys (flares). Initial flares, composed mainly of $Mg/NaNO_3$, were relatively ineffective since the emissivity of MgO, its main combustion product, is low compared to blackbodies. Simply speaking, the flare does not radiate well and therefore is not an attractive target for the seeker. Subsequent CM system development focused on generating large amounts of heat and extensive use of carbon black, since carbon black behaves much like a blackbody. The emissivity of carbon black is about 20 times

_____

The journal model is *Journal of Propulsion and Power*.

greater than that of MgO, translating into radiant behavior much closer to the ideal blackbody and a more effective CM. Today, flares remain the most commonly used passive countermeasures due in part to inexpensive components, ease of handling and reliability.

As CM systems matured, missile designers developed ways to nullify the improved countermeasures. IR counter-countermeasures (IRCCM) allow missiles to detect the presence of flares and reject them as valid targets. IRCCM consist of two fundamental parts: the *trigger*, which detects the flare, and the *counter*, which takes a designated action to reject the flare. There are several types of triggers: rise time (temporal), two-color (spectral), kinematic, and spatial, as well as several types of counters: simple memory, seeker push-ahead, seeker push-pull, sector attenuation, electronic field-of-view gating, and time phase blanking[3].

Todays IRCCM are more advanced than ever. Regardless of which trigger and counter employed, most CM are accurately detected and rejected. Thus, new methods for increased effectiveness of current inexpensive CM must be developed. If the heat produced by the target can be reduced, then IR seeker will be more inclined to track flares rather than aircraft. This can be accomplished simply by reducing the thermal signature of the aircraft *hot spots*.

A. Research Objectives

The primary goal of the present research is to determine the feasibility of reducing the thermal signature of a jet engine by injecting liquid nitrogen (LN_2)and water into the exhaust stream; secondary goal is to determine how this injection would effect the acoustic signature. Ultimately, a foundation will be laid for future research in this area.

To effectively accomplish the above objectives, research was conducted on two fronts. First, numerical simulations were preformed with FLUENT for comparison with experimental results. Second, experimental investigations were performed. A liquid nitrogen injector manifold was designed and fabricated based on parameters determined from the simulations. The manifold was mounted aft of the nozzle of the research turbojet in the Texas A&M University (TAMU) Propulsion Lab. Several rounds of experiments were preformed and compared to results from part one of the research. Data taken during the experiments include temperature measurements via thermocouples, maximum sound levels, and thermal images via a FLIR Systems$^{\mathrm{TM}}$P60 thermal imaging system.

B. Thesis Outline

This thesis consists of six chapters: The current chapter offers a brief introduction and sets the main research objectives. Chapter II introduces the fundamental types of IR seekers, laws of radiation, and discusses other relevant issues related to IR radiation and molecular kinetics. Numerical simulations are discussed in Chapter III and Chapter IV presents the original experiment design and explains the subsequent modifications and secondary experiments. Chapter V presents and compares the results from the simulations and experiments. Finally, Chapter VI concludes the thesis with observations about the present research and offers recommendations on related future work.

CHAPTER II

IR SEEKER TECHNOLOGY

This chapter begins by briefly describing the fundamental types of IR seekers and how they work. Next, it explains the physics associated with the IR technology and why liquid nitrogen injection is not the ideal solution for shielding the IR emission of a jet engine.

A.   Fundamental IR Seekers

There are three main types of IR seekers: spin-scan, conical-scan, and imaging[3]. The simplest of these is the spin-scan seeker with amplitude modulation (AM) tracking. It consists of four basic components: the optics, the reticle, the sensor element and assorted filters (Fig. 1). Energy emitted by the target (source) is focused by optics and passed through a spinning reticle, producing a modulated (pulsed) signal that impinges on the sensor element. Output from the sensor is fed through various filters, where the signal is conditioned by removing information regarding extended sources (e.g. clouds), the frequency of the spinning reticle, etc. The resulting output signal is the tracking error in the form of a sine wave. The amplitude and phase of this wave corresponds to the magnitude and direction of the tracking error, which is subsequently fed to the guidance subsystem.

Conical-scan (con-scan) seekers function similarly to spin-scan seekers, but are somewhat more advanced. Con-scan seekers focus gathered energy through the outer edge of a stationary reticle to the IR sensor via a secondary spinning mirror. This mirror is tilted with respect to its rotational axis (Fig. 2). The sensor outputs a frequency modulated (FM) sine wave which is first fed through a frequency discriminator before passing through various filters to produce the tracking error.
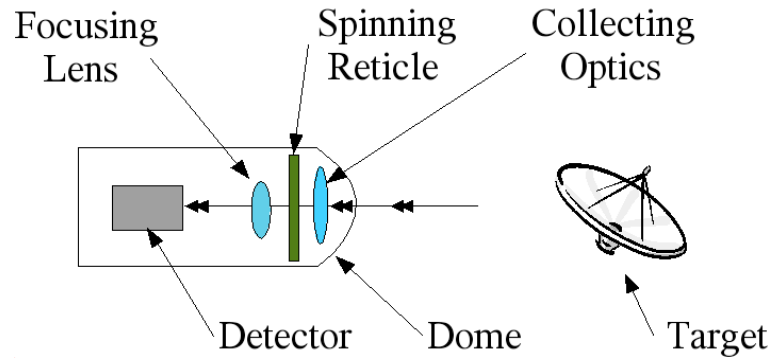
Fig. 1. Basic elements of a spin-scan seeker head.
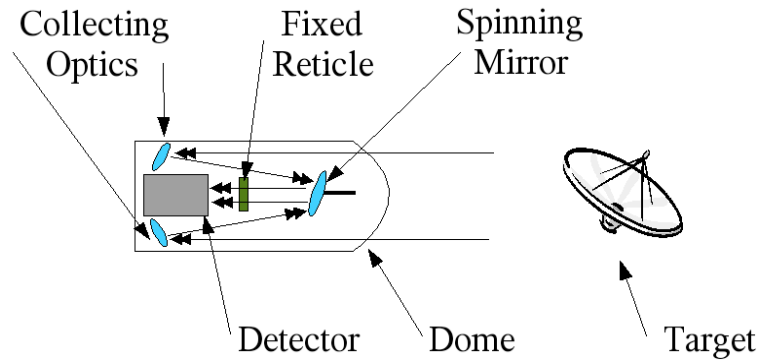
Fig. 2. Basic elements of a con-scan seeker head.

The third main type of seeker is the imaging seeker. This is the most advanced seeker, and uses an array of sensor elements called a focal plane array (FPA) instead of a single reticle. From the detector array output, a spatial map of the scene is built and passed to processing software. Due to sophisticated software, imaging seekers can readily distinguish between aircraft, clouds, birds, flares, etc. and are not easily fooled by CM. Figure 3 shows a representation of a target on an FPA.
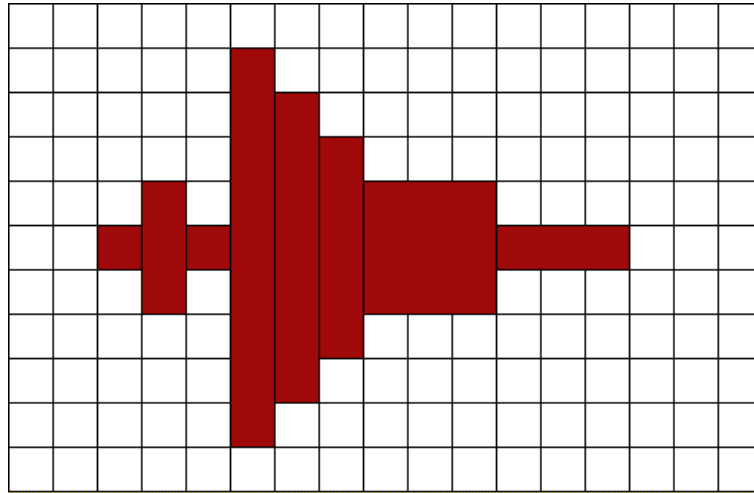
Fig. 3. Representation of a target as seen by a focal plane array.

B. Laws of Radiation

Thermal radiation refers to the electromagnetic (EM) radiation (EMR) emitted by an object based solely on its temperature. The "thermal" region of the EM spectrum is generally considered to extend from the short wave ultraviolet (UV) to the long range IR (Fig. 4)[2]. The sensor element in a typical IR seeker is generally sensitive only
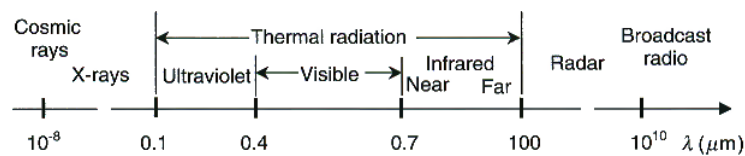
Fig. 4. The electromagnetic spectrum (Taken from Mahan[2]).

to select radiation bandwidths. For example, lead sulfide (PbS) detector elements are sensitive to the 2-3 μm range, designated $\alpha - band$, and lead selenide (PbSe) detector

elements are sensitive to the 3-5 μm range, designated $\beta - band$[4]. Both the PbS and the PbSe detector elements are sensitive only to radiation in select IR bands. Other sensors will be sensitive to other bandwidths. For example, the retina of the human eye contains photoreceptors that are sensitive only to EMR in the visible band (0.4-0.7 μm).

Each band corresponds to a temperature range which can be quantified using *Wien's displacement law*. Wien's law states that the wavelength of peak energy emission of a blackbody is inversely proportional to its absolute temperature.

$$\lambda_{max} = \frac{2897.756 \mu m \cdot K}{T[K]} \tag{2.1}$$

As previously mentioned, the peak sensitivity of a typical uncooled PbS detector lies in the 2 μm range. To determine the temperature of the radiator with a corresponding peak energy emission wavelength of 2 μm, one uses Wien's displacement law.

$$T = \frac{2897.756 \mu m \cdot K}{\lambda_{max} \mu m} = \frac{2897.756}{2} = 1448.88 K \tag{2.2}$$

Typically aircraft engines operate with turbine inlet temperatures ranging from 1200-1500 K, thereby emitting thermal radiation at wavelengths from 1.9-2.1 μm. This clearly illustrates the suitability of PbS detectors for homing in on the hot tail pipes of jet aircraft.
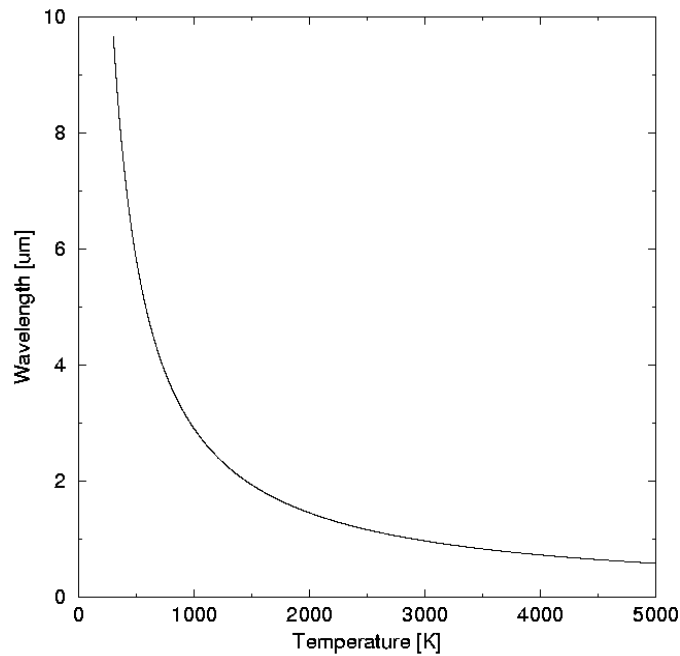
Fig. 5. Variation of peak energy wavelength with absolute temperature.

Figure 5 indicates that as the temperature decreases, the peak of the emitted radiation shifts toward longer wavelengths. The implied result is that by reducing the operating temperature of the engine, it may be possible to shift the wavelength of IR radiation out of the detectable range of certain seekers. Realistically, an engine cannot be sufficiently cooled for this purpose. It would be terribly inefficient at best, and most likely the engine would not function.

The above train of thought may lead one to assert that by simply cooling the exhaust plume, the IR signature of the engine may be masked. While sounding reasonable, the supporting argument that follows is incorrect.

By rapidly reducing the temperature of the exhaust plume immediately behind the nozzle, one can shift the wavelength out of the range of IR seekers. This technique, when combined with other CM, can increase survivability by making pyrotechnic decoys appear more attractive to IR seekers.

$$\lambda_{max} = \frac{2897.756\mu m \cdot K}{T[K]} = \frac{2897.756}{1200} = 2.415\mu m \qquad (2.3)$$

$$\lambda_{max} = \frac{2897.756\mu m \cdot K}{T[K]} = \frac{2897.756}{1000} = 2.898\mu m \qquad (2.4)$$

By cooling the exhaust gasses about 200 K, the peak emission wavelength is shifted by 0.4 μm and a 400 K temperature reduction shifts the peak emission wavelength by nearly 0.9 μm.

The above explanation is only true if the exhaust plume is a solid object radiating like a blackbody. To understand why, one must examine the interaction of EMR and gaseous mixtures.

C.   IR Detection and Propagation through Gasses

IR detection is a passive process of collecting and measuring thermal radiation emitted by a distant target. To develop a method for avoiding detection, one must first understand how EMR propagates through gaseous mixtures, specifically the atmosphere, and the major factors that influence detector operation.

The total amount of thermal power radiated by a source is characterized by the rate of energy flow per unit time. This is called the energy flux, F, and has the same units as power.

The flux per unit area at the detector is called the incidence, E, and the flux per unit area of the source is called the exitance, M. For thermal radiation, the exitance

is given by the *Stefan-Boltzman Law,*

$$M = \epsilon \sigma T^4 \tag{2.5}$$

where ϵ is a dimensionless property of the radiating surface called the emissivity, σ is the Stefan-Boltzman constant $(5.6696 \times 10^{-8} W/(m^2 K^4))$, and T is the absolute temperature of the radiating surface in K.

To relate incidence and exitance some assumptions must be made. Considering only a long-range source, one can assume the thermal radiation is effectively emanating from a single point (Fig. 6). A point source will radiate with complete spherical symmetry thereby geometrically relating exitance to incidence by $\pi R^2/4$. The final transfer function is then

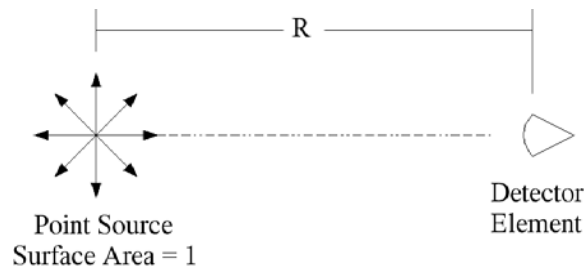$$E = \left(\frac{1}{4}\pi R^2\right) M \tag{2.6}$$

Fig. 6. Point source and single detector element schematic.

The above transfer equation is idealized in the sense that it does not directly account for the energy lost to the atmosphere. IR energy is generally lost to the atmosphere in four ways: absorption, scattering, photochemical reactions, and photoionization[1].

Scattering is simply the energy loss due to redirection away from the detector. Absorption is the energy loss due to vibration and rotation of molecules. Photochemical reactions generally involve only ultraviolet and visible radiation. Photoionization requires high energy photon and is usually only associated with wavelengths shorter than 0.1 μm. Therefore, only absorption and scattering will be considered here. The overall energy loss is called attenuation and is primarily a function of the wavelength and range, but is also dependent on the properties of the atmosphere (e.g. humidity, composition, visibility).

An isolated gas molecule can store energy in various forms. Most of this energy is stored as kinetic energy and electrostatic potential energy of its electrons moving about the nuclei. Lesser amounts of this energy are associated with atoms vibration about their mean position and rotation of the molecule about its center of mass[1]. Quantum mechanics maintains that these energy levels can only change in specific configurations of electron orbits, vibrational frequencies and amplitudes, rotation rates, vibrational and rotational modes, etc. Quantum theory also treats the energy transmitted by EMR as discrete particles called photons. The energy associated with a photon is calculated by $W = h\nu$, where h is Planck's constant ($6.6260755 \pm 0.0000040 \times 10^{-34} J \cdot s$), and ν is the frequency of the EMR. Photons travel at the speed of light $c(2.99792458 \times 10^{10} cm \cdot s^{-1})$, thus the frequency and wavelength are related by $\nu = c/\lambda$. Quantum theory is beyond the scope of this work. It is only necessary to be aware of these concepts and understand that quantum theory sets the *rules* molecules must follow when absorbing IR energy.

Based on the rules of quantum mechanics, only those molecules that have a dipole (CO_2, H_2O, O_3) are significantly excited by IR radiation. When a dipole absorbs IR radiation, a portion of the energy is converted to heat by the vibratory and/or rotational motion of the molecule. The remaining energy is then re-emitted, usually

at longer wavelengths.

Table I. Typical atmospheric constituents below 100 km[1].

Constituent	Fraction of total molecules
Nitrogen, N_2	0.7808
Oxygen, O_2	0.2095
Argon, Ar	0.0093
Water vapor, H_2O	0-0.04
Carbon dioxide, CO_2	325 ppm
Neon, Ne	18 ppm
Helium, He	5 ppm
Krypton, Kr	1 ppm
Hydrogen, H	0.5 ppm
Ozone, O_3	0-12 ppm

The wavelength(s) at which the atmosphere absorbs IR energy affects attenuation. Typical atmospheric constituents, shown in Table I, will absorb radiation at different wavelengths. Since N_2 and O_2 are diatomic molecules, they have no unbalanced charges and are relatively unaffected by IR radiation. CO_2, O_3 and H_2O, on the other hand, have unbalanced charge distributions and readily absorb IR radiation. So, although the atmosphere contains substantially less CO_2, O_3 and H_2O, than N_2 and O_2, they are the primary contributors to attenuation.

The amount of attenuation influences Equation 2.6 through the range, R. The total energy lost depends on the total amount of energy transmitted and over what distance. Generally speaking, high flux and long range transmission correspond to high loss. *Bouguer's Law* quantifies the flux remaining after attenuation as a function of the range.

$$\tau = e^{-BR} \tag{2.7}$$
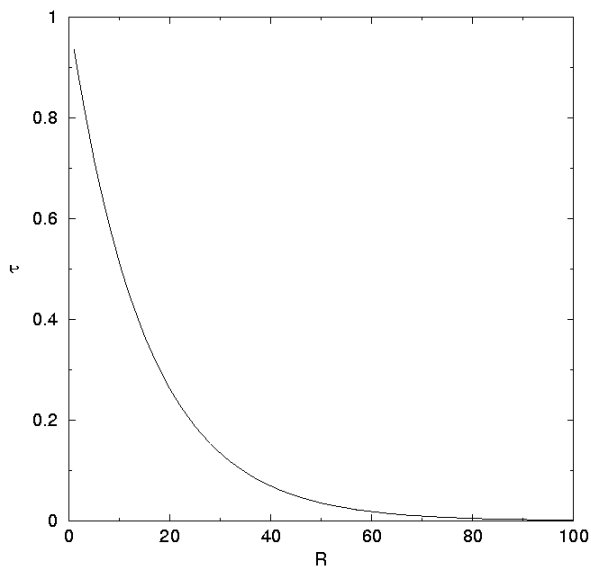
Fig. 7. Transmission coefficient versus range to target.

B is the extinction coefficient and is a property of the specific detector. For the $\beta - band$, B is typically $6.7 \times 10^{-5} m^{-1}$. τ is the dimensionless transmission coefficient and is the fraction of the energy flux remaining after attenuation. Figure 7 illustrates that as τ goes to zero the distance between the target and the detector increases.

The transmission coefficient is inserted directly in the transfer equation (Eqn.2.6)

$$E = \left(\frac{\tau}{4}\pi R^2\right) M \qquad (2.8)$$

D. What does it all mean?

The preceding sections have explained how reducing the temperature of an object will increase its wavelength of peak emission. It was suggested that as a consequence of reducing the temperature of the exhaust plume by injecting liquid nitrogen, a shift in wavelength might be possible. It is now clear that this is certainly not the case. The nature of the interaction of EMR and gas molecules in the IR band is considerably different than the interaction of EMR and solid bodies. Based on the rules of quantum mechanics and molecular structure, it is clear that the most abundant molecules in the atmosphere, N_2 and O_2, only slightly affect attenuation, while some of the least abundant molecules, CO_2, H_2O, O_3, greatly affect attenuation.

Simply stated, cooling the exhaust gasses will not work. The IR radiation from the nozzle will penetrate the injected N_2 and still be visible to the seeker. This also makes shielding by N_2 impossible. Flooding the exhaust with H_2O, on the other hand will, quite possibly, create an effective IR shield.

CHAPTER III

NUMERICAL SIMULATION

This chapter begins by introducing general forms of the conservation equations followed by a brief explaination of the specific equations solved in the simulation and the turbulence model. Finally, descriptions of the computational domain and boundary conditions are presented.

A.   Basic Fluid Model

To calculate the properties $(\rho, P, T, \vec{V}, etc.)$ of a compressible flowfield at all points in the flow one solves the basic flow equations. These equations are extensions of three conservation principles: mass, momentum and energy[5]. Expressed in integral form, they are given below.

1. Conservation of Mass *mass can neither created nor destroyed*

$$\frac{\partial}{\partial t} \iiint_V \rho \, dV = - \iint_S \rho \vec{V} \cdot d\vec{S} \tag{3.1}$$

2. Conservation of Momentum *the time rate of change of momentum of a body equals the net force exerted on it* (Newton's second law applied to fluid flow)

$$\frac{\partial}{\partial t} \iiint_V \rho \, dV + \iint_S (\rho \vec{V} \cdot d\vec{S})\vec{V} = \iiint_V \rho \vec{f} \, dV - \iint_S P \cdot d\vec{S} \tag{3.2}$$

3. **Conservation of Energy** *energy can neither be created or destroyed* (Eqn. 3.2 does not include shaft power, work done by viscous stresses, or thermal conduction, diffusion, or radiation.)

$$\frac{\partial}{\partial t}\iiint_V \left[\rho\left(e + \frac{V^2}{2}\right)\right]dV + \iint_S \left[\rho\left(e + \frac{V^2}{2}\right)\right]\vec{V}\cdot d\vec{S}$$
$$= \iiint_V \dot{q}\rho\, dV - \iint_S P\vec{V}\cdot d\vec{S} + \iiint_V \rho(\vec{f}\cdot\vec{V})\,dV \tag{3.3}$$

The commercial computational fluid dynamics (CFD) package FLUENT solves the conservation equations in the following differential form[6]

$$\frac{\partial\rho}{\partial t} + \frac{\partial}{\partial x}(\rho v_x) + \frac{\partial}{\partial r}(\rho v_r) + \frac{\rho v_r}{r} = S_m \tag{3.4}$$

$$\frac{\partial\rho}{\partial t}(\rho\vec{V} + \nabla\cdot(\rho\vec{V}\vec{V}) = -\nabla P + \nabla\cdot\bar{\bar{\tau}} + \rho\vec{g} + \vec{F} \tag{3.5}$$

$$\frac{\partial\rho}{\partial t}(\rho E) + \nabla\cdot(\vec{V}(\rho E + P)) = -\nabla(k_{eff}\nabla T + \bar{\bar{\tau}}_{eff}\cdot\vec{V}) \tag{3.6}$$

where, v_x and v_r are the axial and radial velocities respectively, P is the static pressure, $\bar{\bar{\tau}}$ is the viscous stress tensor given by Equation 3.7 and E is total energy given by Equation 3.8.

$$\bar{\bar{\tau}} = \mu\left[\left(\nabla\vec{V} + \nabla\vec{V}^T\right) - \frac{2}{3}\nabla\cdot\vec{V}\bar{\bar{I}}\right] \tag{3.7}$$

$$E = h - \frac{P}{\rho} + \frac{V^2}{2} \tag{3.8}$$

Gravitational and external body forces are accounted by $\rho\vec{g}$ and $\vec{F}$, μ is the molecular viscosity, $\bar{\bar{I}}$ is the identity tensor and S_m is an *added mass* term used by FLUENT[6]. These are coupled to the turbulence model transport equations through the effective conductivity, k_{eff}, and the effective viscous stress tensor, $\bar{\bar{\tau}}_{eff}$.

To produce a mathematically determinate system, Equations 3.4 through 3.6 must be supplemented with several additional relations and an appropriate turbulence model. Compressible flow is basically characterized by Mach number, total pressure and total temperature. Thus, the number of unknowns may be reduced by exploiting the definition of Mach number, M, the speed of sound, c, the ratio of specific heats, γ, and the ideal gas law for compressible flow. In the relations shown below, P_{op} is the operating pressure, P is the local static pressure, R is the universal gas constant, M_w is the molecular weight and T is the static temperature.

$$
\begin{aligned}
M &= v_x/c \\
c &= \sqrt{\gamma RT} \\
\gamma &= c_p/c_v \\
\rho &= \frac{P_{op} + P}{\frac{R}{M_w}T}
\end{aligned}
$$

To relate static pressure and temperature to total pressure and temperature, the following isentropic relations are used.

$$
\begin{aligned}
\frac{P_o}{P} &= \left[1 + \frac{\gamma - 1}{2}M^2\right]^{\gamma/\gamma - 1} \\
\frac{T_o}{T} &= 1 + \frac{\gamma - 1}{2}M^2
\end{aligned}
$$

The task of choosing an appropriate turbulence model can be quite cumbersome, and the details are beyond the scope of this discussion. One can simplify things by choosing a conventional model typically used for practical engineering problems. One such model, the Wilcox[7] variation of the standard $k-\omega$ model, is used in the present simulation. The $k-\omega$ turbulence model adds two transport equations to calculate turbulence kinetic energy, k, and specific dissipation rate, ω [6].

Combining the flow equations (Eqn. 3.4 through 3.6) with the above relations and a turbulence model produces a closed system from which the flow properties can be attained.

B. Domain Model and Boundary Conditions

The cylindrical control volume for the present simulation extends downstream from the nozzle exit to the exit of the exhaust duct, with a radius equal to the inner diameter of the exhaust duct. The three flow inlets include the engine exhaust, airflow around the engine and injector manifold (bypass airflow), and injected liquid nitrogen (LN_2). Taking advantage of the physical symmetry, the computational domain was modeled in GAMBIT using a two-dimensional, axisymmetric domain as shown in Figure 8.
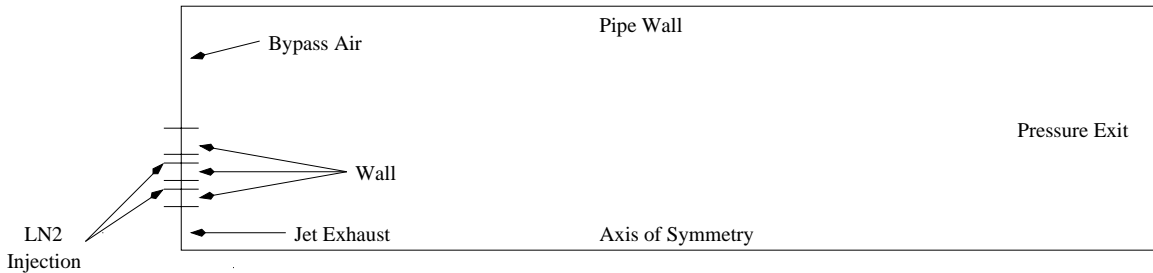

Fig. 8. Computational domain boundary conditions.

The left boundary of Figure 8 represents all inlet boundaries to the domain. The first inflow boundary is the jet exhaust modeled as a pressure inlet with total pressure set to 1.398 bar and total temperature set to 861 K. Continuing up the left boundary, is the LN_2 injector manifold modeled in five segments: three adiabatic wall segments and two pressure inlets (the injector ports). Total pressure for the injectors is set to

15 *bar* and total temperature is set to 73 *K*. The final inlet boundary is the bypass airflow defined as a velocity inlet, with static temperature set to 300 *K*, and velocity set to 15 *mps*. The upper boundary is the adiabatic wall boundary of the exhaust pipe. The entire right boundary is the domain exit and is modeled as a pressure exit with static pressure set to 1 *bar*. Finally, the lower boundary is the axis of symmetry. An example coarse mesh is shown below in Figure 9.
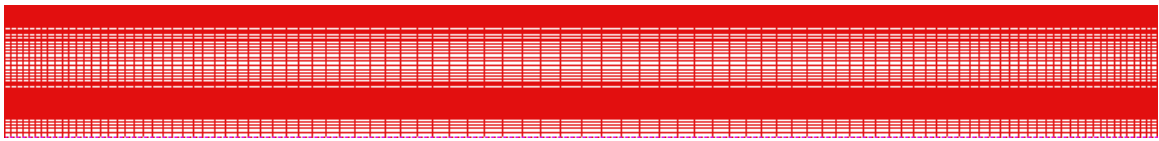

Fig. 9. Computational domain with coarse mesh.

CHAPTER IV

EXPERIMENT DESIGN

This chapter begins by outlining the development of the facilities and equipment used in the original experiment. Next, an explanation is given of the modifications made to the original experiment leading to subsequent experiments. Finally, an overview of several re-engineered engine components is presented.

A.   Original Experiment and Facility Improvements

Substantial modifications and additions to the TAMU Propulsion Lab Test Cell were made throughout this research. The most invasive of these was the new exhaust duct. Additionally, various instrumentation and associated hardware and software was also purchased. This equipment includes thermocouples, cryogenic hardware, data acquisition components, dosimeter, a digital video camera, and related software.

1.   Exhaust Duct

Previously, the test cell had no means for collecting thermal measurements in the jet exhaust. Any modifications to the original exhaust pipe would be expensive and irreversible due to the extensive acoustic and heat insulation. Therefore, a new exhaust pipe was designed and fabricated to meet the requirements of the present research. Specifically, the new exhaust duct includes strategically placed thermocouple taps, an IR sightglass viewport for thermal imaging and windows for visual access.

The exhaust duct is composed of seven flanged sections built from standard 22 inch schedule 40 steel pipe. The five central sections measure 12 inches overall length (oal), with three of the sections featuring two 8 inch by 12 inch flanged window openings. The section bolted directly to the turbojet enclosure measures 16 inches
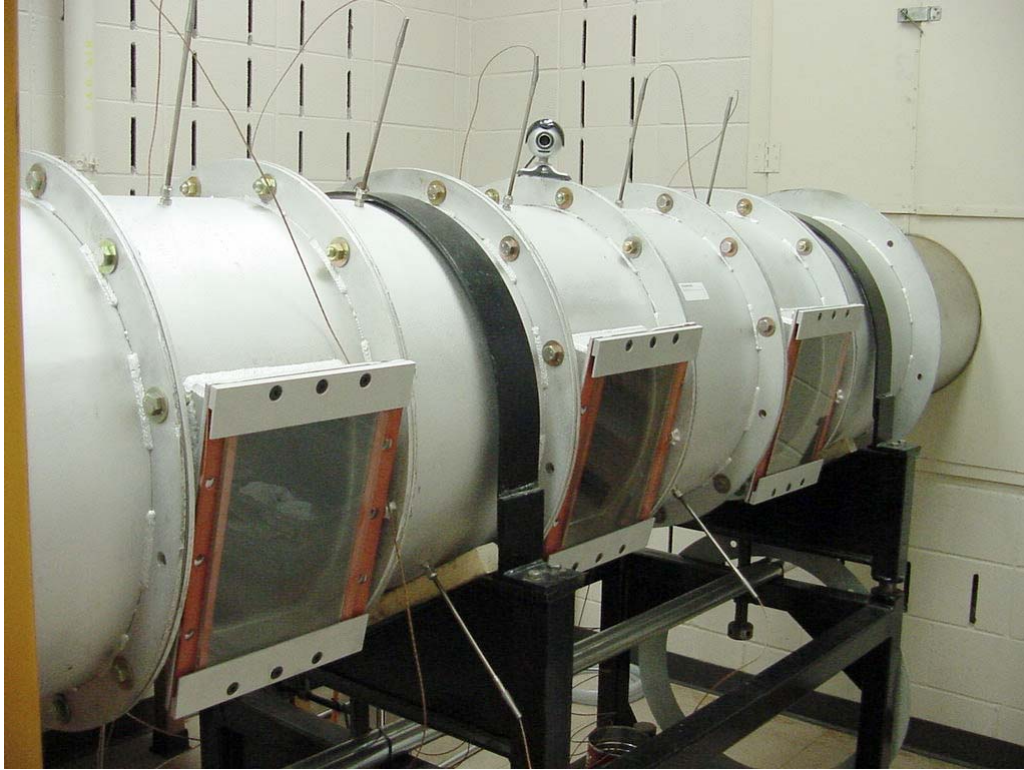
Fig. 10. Exhaust duct.

oal due to the 4 inch protrusion into the enclosure. The last section measures 17 inches oal and has a different flange on one end to connect the duct to the outside exhaust stack. When fully assembled the duct is roughly 8 *ft* long, 22 inches in diameter and weighs about 650 *lb* (Fig. 10). Due to the scale of the components, the exhaust duct fabrication was contracted to Croft Construction Company in Dayton, Texas. Working drawings are included in Appendix A.

2. Instrumentation

All data acquisition (DAQ) hardware and software was purchased from National Instruments to meet the requirements of this research and serve the general instru-

mentation needs of the test cell. A single Pentium II PC, running Windows 2000 and LabVIEW 7 records temperature data from the fourteen, twelve inch long, *k-type* Thermosensors thermocouples (TCs) and controls the LN_2 flow via a solid state relay and a Parker Gold Ring solenoid valve.

Three TCs were installed at 120° in each the solid exhaust duct sections and two TCs were installed at 180° in each of the windowed sections. Figure 10 shows seven of the fourteen TCs protruding from the exhaust duct. The TCs are wired in differential configuration to a pair of TBX-68 terminal blocks (Fig. 11). The terminal blocks are linked to the multifunction DAQ board via a special 2 *m* shielded cable.
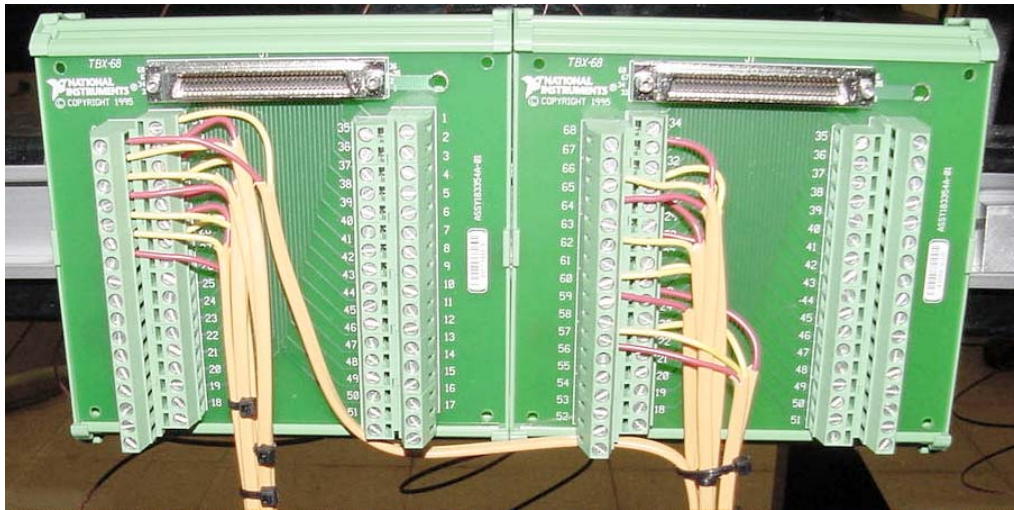

Fig. 11. TBX-68 wired for differential thermocouples.

The LabVIEW program is a simultaneous dual loop control structure which runs continuously until user termination. The first loop, shown in Figure 12, records and displays TC data while the other loop, shown in Figure 13, controls the LN_2 injection sequence.

The TC loop constantly samples the signal from each thermocouple in sequence at a predefined sampling rate. Once the set number of samples are read, they are averaged, the gauges are updated and the average temperature values are written to the designated output file. Since temperature fluctuations in the exhaust occur over several seconds, averaging the samples over a comparably short interval (approx. 0.5 s) is a simple and effective means of reducing the number erroneous temperature readings without sacrificing measurement accuracy.

Fig. 12. LabVIEW screenshot: thermocouple loop.

The LN_2 injection control loop constantly monitors the injection initiation switch located on the control panel. When activated, the loop waits a predetermined number of seconds, then sends the signal to open the LN_2 solenoid valve and starts an elapsed

time clock. Once the injection duration time is reached, the open signal is terminated and the LN_2 solenoid closes.

Temperatures are monitored from the *Thermocouple Display and DAQ Control Screen* via digital displays and gauges (Fig. 14). In addition to monitoring temperature readings, from this screen the operator can adjust the sampling rate, number of samples to average, set the output file name and completely control the LN_2 injection sequence timing.
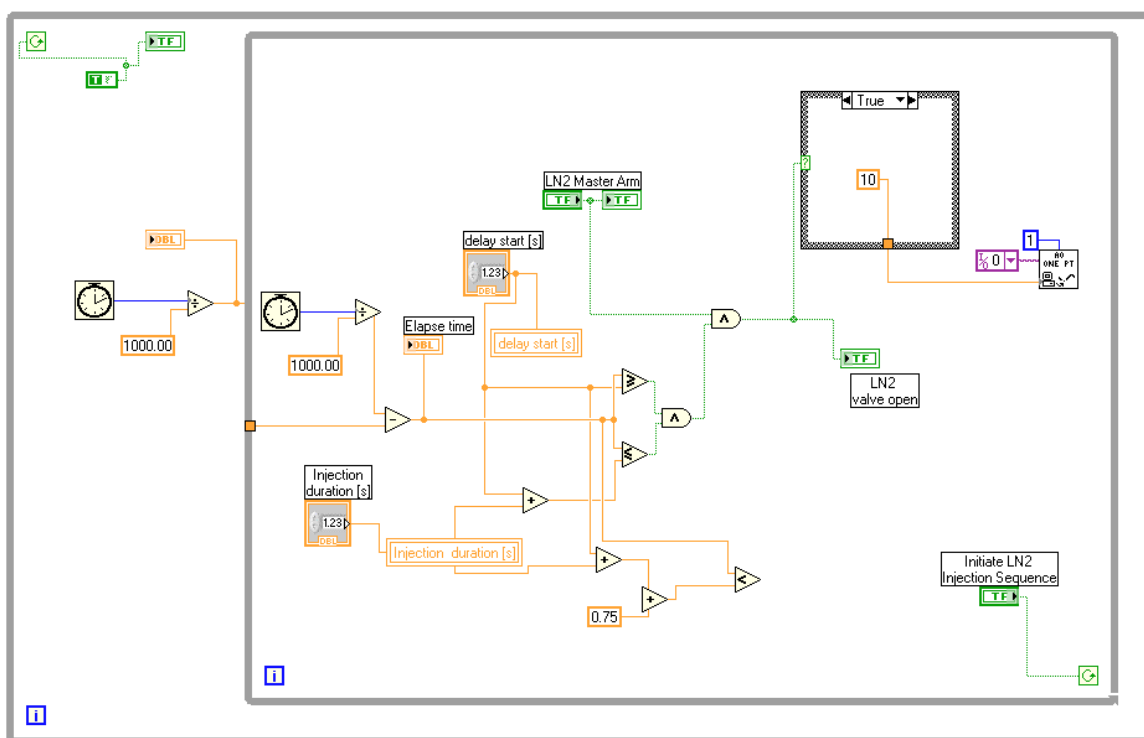

Fig. 13. LabVIEW screenshot: LN_2 injection loop.
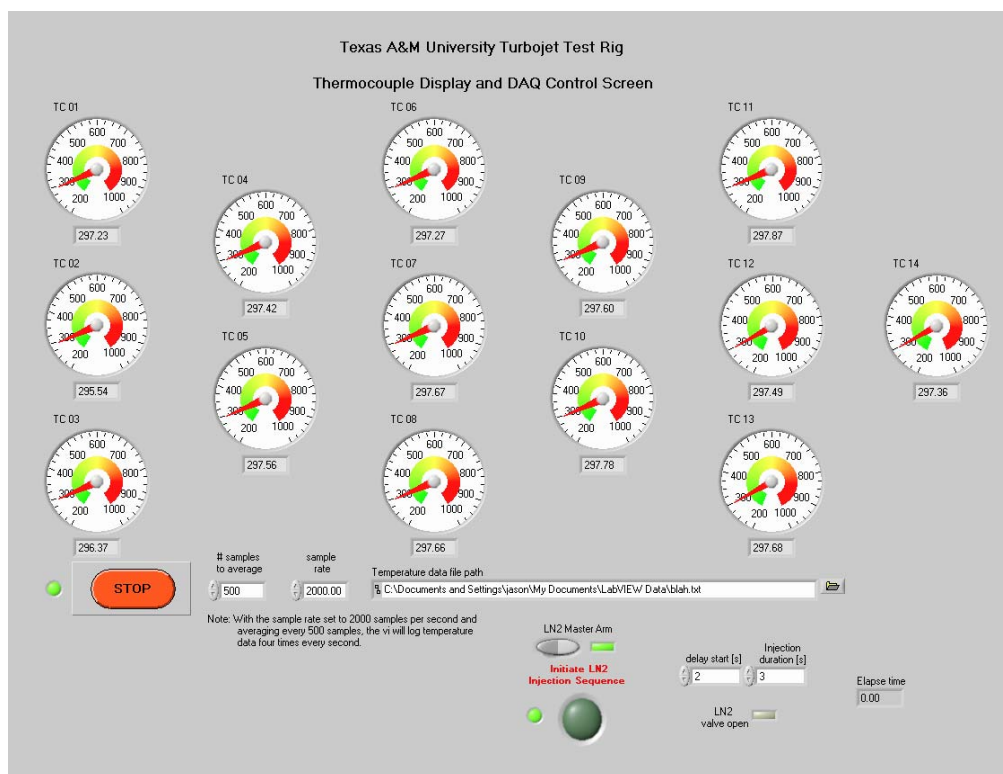
Fig. 14. LabVIEW screenshot: DAQ control screen.

3. Injection Manifold

The second major component of the original experiment is the injection manifold(Fig. 15).
The injection manifold face plate is a 12 inch square aluminum plate 0.5 inches thick.
In the center of the plate is a 5.25 inch diameter through hole for unrestricted flow of
the exhaust gasses. Injector ports are located on radii of 3.0 inches and 3.213 inches
from the plate center. The ports are arranged in two concentric series of 128 equally
spaced 0.0313 inch diameter holes. LN_2 enters the manifold via a 0.5 inch diameter
stainless steel hose through a single connection on the rear plate. The two plates are
sealed with a 0.0625 inch thick Teflon^{TM}gasket and twelve 1/4-20 UNC socket head
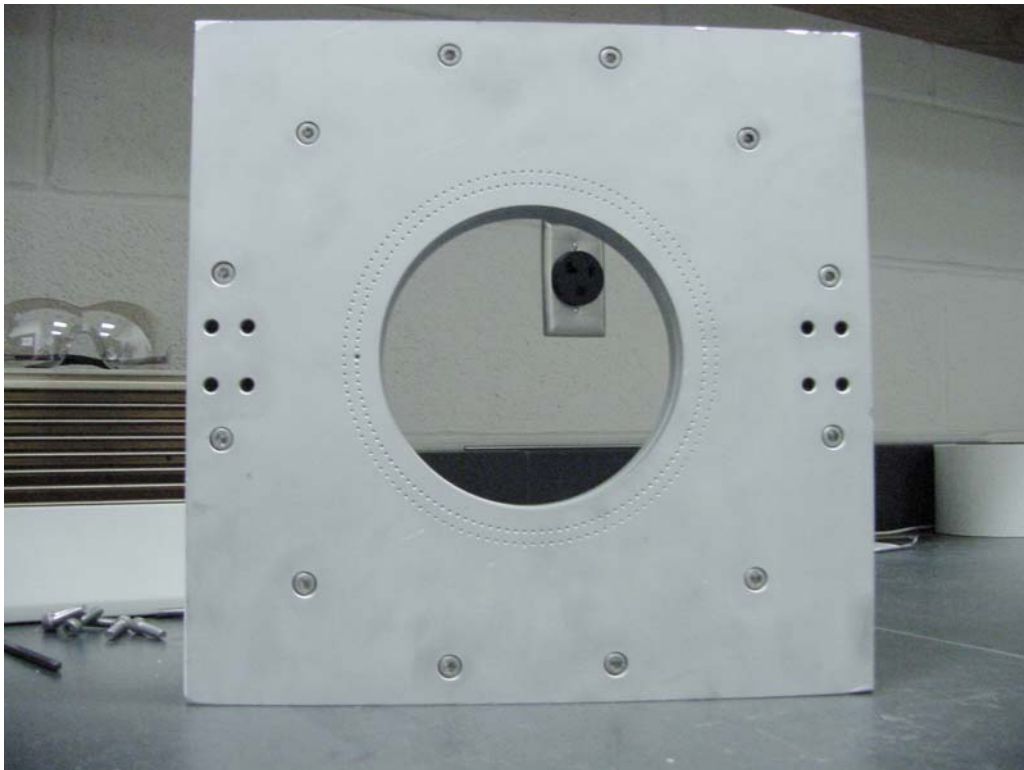cap screws equally spaced on an 11 inch bolt circle.

Fig. 15. Injection manifold.

4.   IR Mirror

The last major component built specifically for this research was the IR mirror. This mirror facilitates the required aft view of the engine for thermal imaging. The second window on the starboard side of the exhaust duct was replaced with a 0.5 inch thick carbon steel plate. Mounted at the center of this plate, outside the pipe, is a 2 inch Hawk IR infrared sightglass. Centered about the sightglass on the opposite side of the plate is the aft looking stainless steel mirror. An exploded view of the mirror solid model is shown in Figure 16.

The three main supports of the mirror assembly were machined from 0.625 inch thick aluminum plate and feature slots for mirror adjustment. The mirror is secured in a aluminum frame and bolted to the back support. The angle of the mirror may be fine tuned by inserting shims between the frame and the back plate. The entire IR mirror assembly is secured to the steel plate with eight 3/8-16 UNC socket head cap screws from outside the pipe.

B.   Secondary Experiments and Equipment

Once it became clear that cooling the exhaust by injecting LN_2 would not, by itself, change the temperature reported by the FLIR camera, it was decided to attempt shielding the IR signature with water.

A simple experiment was designed and built to validate the idea. An elevated water reservoir with a rectangular slot cut into the bottom produces a water sheet about 0.0625 inch thick between a heated carbon steel plate (3.25x3.25x0.125 inches @ 500 C) and the FLIR camera. The quick experiment verified that a thin water sheet could completely block the IR energy emitted by the hot plate. To show the effects of the emissivity of different materials on the temperatures reported by the
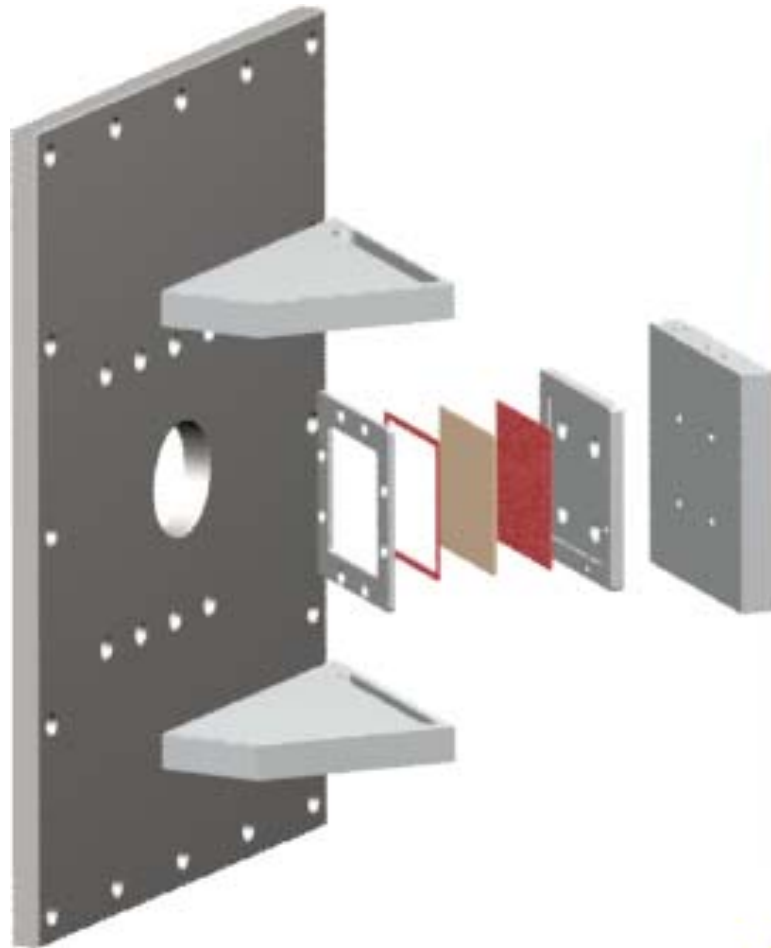
Fig. 16. Mirror solid model exploded view.

FLIR camera, a thin layer of gold was electroplated on one half of the steel plate and the experiment was repeated.

Following the water sheet shielding experiments, a single hole probe was built to inject water into the exhaust stream. From the probe base to the center of the tip is 11 inches, positioning the injection at the center of the exhaust stream. The hole diameter of the probe tip is 0.125 inch. Through the probe, water was injected against the exhaust stream at a mass flow rate of 0.266 kg/s. The plumbing was then rerouted to connect the injection manifold to the test cell water supply and water was injected through the manifold with the exhaust stream at a mass flow rate of 2.36 kg/s.

C.   Re-engineered Components

During the course of the research, several engine components failed. These failures were primarily due to age and life expectancy of the engine. The turbojet engine used for this research was manufactured by Noel Penny Turbines (NPT) Limited sometime in the late 1970s. The NPT401 was originally designed for use in target drones. The British company apparently stopped trading in the late 1980s and finally folded in 1990. As such, replacement parts are no longer available for these engines and must be build as needed. Each of the failed components were redesigned for durability and ease of fabrication and are presented here.

1.   Starter

The first failed component was the starter motor. Originally, the NPT401 used a modified Lucas B90 brushed dc electric motor. The B90 was underpowered and frequently burned up. Several attempts were made to develop a pneumatic solution to

start the engine. These designs ranged from Pelton style turbines to simple modifications of an inexpensive impact wrench. None of the pneumatic designs produced enough torque to reliably start the engine. Finally, a 6.6 *Hp* 3-phase arbor motor was purchased and installed.
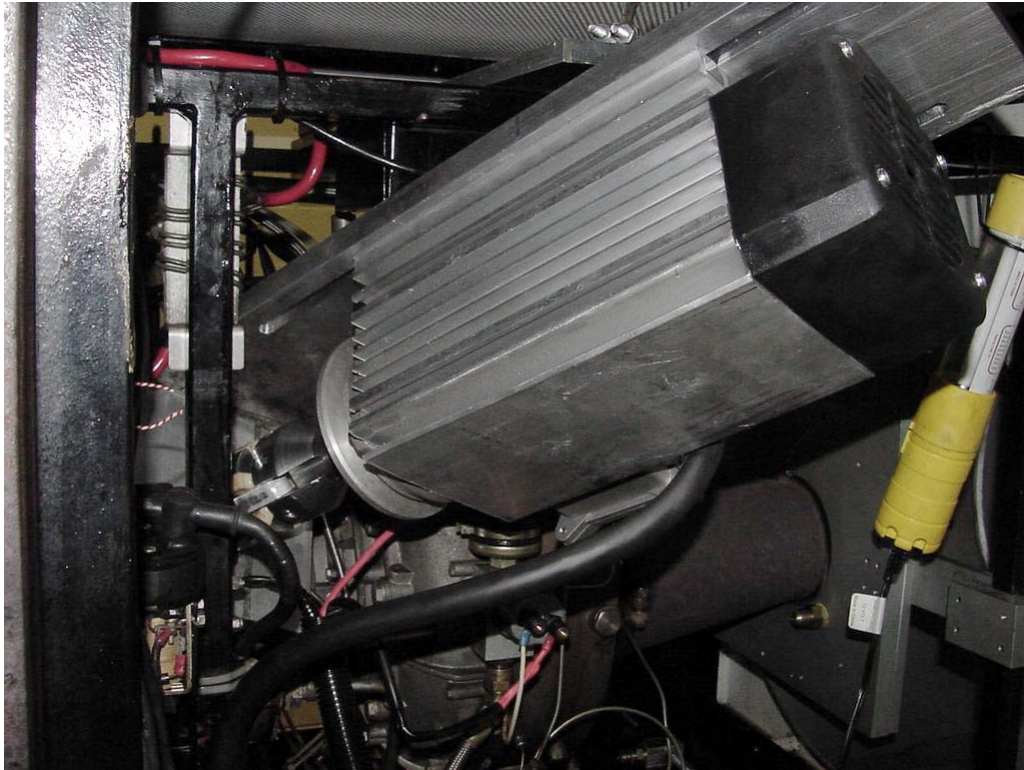

Fig. 17. Small starter motor installed on turbojet.

The large arbor motor performed well for several months, but because of its weight (approx. 71 *lb*), produced very large stresses on its connection to the engine compressor. These stresses ultimately lead to failure at the connection. It was decided that the motor was too large to adequately support in the engine enclosure and a smaller motor was needed.

A 2.4 *Hp* 3-phase motor was purchased and installed (Fig. 17). The smaller motor (approx. 42 *lb*) reduced the amount of necessary support while still providing the torque required to start the engine.

2. Clutch

The second failed component was the clutch between the starter motor and the turbojet's compressor. The original clutch was a light duty roller ramp style clutch with four rollers. Figure 18 shows the damaged clutch components after several rebuilds. Major wear and failure indicators can be seen on all components: 1/ burn marks on cage (bottom right) 2/ broken springs and worn plungers (bottom center) 3/ rollers showing excessive wear (middle center) 4/screws with severe shearing damage 5/ damage to outer race components (top left and right)

The damage to the outer race upper and lower surfaces is likely the main cause of the recurring clutch failure. The scarring in these surfaces catch the edges of the rollers, jerking them out of alignment and causing additional damage.

After careful consideration, a more simple centrifugal style clutch design was implemented (Fig. 19). The body of this clutch was machined from a solid piece of stainless steel and is threaded to accept the shaft of the starter motor. It features three aluminum fingers which engage a mating component directly connected to the turbojet's compressor. At about 10,000 *rpm* the centripetal force breaks the connection between the fingers and the mating piece, the fingers swing out their pivot pins and are locked in place via spring loaded arresting pins. The working drawings are included in Appendix B. The drawings have been updated and do not precisely reflect the design presented in Figure 19.

Fig. 18. Original clutch components.

3. Clutch/Compressor Interface

The third failed turbojet component was the interface between the clutch and the compressor. This failure was primarily due to high stress on the bosses caused by the heavy starter motor. After the bosses fractured, the sleeve bearing and rubber seal were subjected to the entire weight of the starter motor (approx. 71 *lb*) as well as the impact of the clutch fingers on the mating piece. The resulting damage is shown in Figure 20.

A new design was developed, strengthening the areas where the interface failed previously. First, the thickness of the material surrounding the bosses was increased

Fig. 19. Redesigned clutch.

allowing the piece to perform under greater load. Second, the sleeve bearing and rubber seal were replaced with a pair of oil cooled roller bearings. The roller bearings solved two persistent problems in the previous design: (1) excessive oil leakage through the sleeve bearing is minimized by using roller bearings and (2) 'wobble' in the shaft is eliminated by using two roller bearings instead of a single sleeve bearing. A cross section of the new interface is shown in Figure 21.

Fig. 20. Damaged interface.
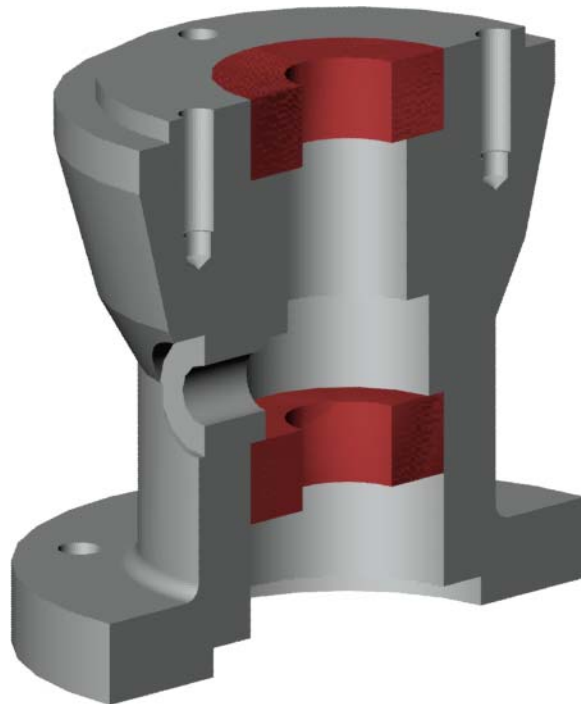
Fig. 21. New interface design cross section (roller bearings shown in red).

CHAPTER V

RESULTS

This chapter presents quantitative and qualitative results of the experimental and numerical investigations. First, results of the LN_2 injection are outlined. Next, results from the water sheet experiments are presented. Then, data from the water injection from the probe and from the manifold are discussed. Lastly, numerical results are presented.

A. Experimental Results

The experimental part of this research consists of three main avenues. The first is the liquid nitrogen injection. The second is the water sheet tests. The third is the water injection into the jet exhaust through the probe and the manifold.

1. LN_2 Injection

The initial goal of this research was to show that the temperature of the turbojet exhaust could be reduced by LN_2 injection. Figure 22 shows that injecting LN_2 at a mass flow rate of 1.127 kg/s for an extended period will result in a maximum temperature reduction of about 22 degrees at TC 7 that is located about 30 inches down the exhaust duct. TCs 9 through 14 report similar temperature drops and all are at least 30 inches from the point of injection. The figure also shows no apparent temperature change reported by the thermocouples nearest the injection. This is due to TC position and exhaust jet velocity. During injection there was no audible change in the engine noise and the magnitude reported by the dosimeter was approximatly 122 dB.

Although Figure 22 shows that injecting LN_2 decreases the temperature of the

exhaust, this alone cannot prevent (or break) missile lock. There are two problems (1) the temperature change is too small and (2) nitrogen is transparent to IR energy (as previously discussed in Chapter 2). The energy radiated by the nozzle will pass through the nitrogen cloud behind the engine unperturbed so the seeker head still 'sees' its hot target regardless of the temperature of the N_2 cloud.
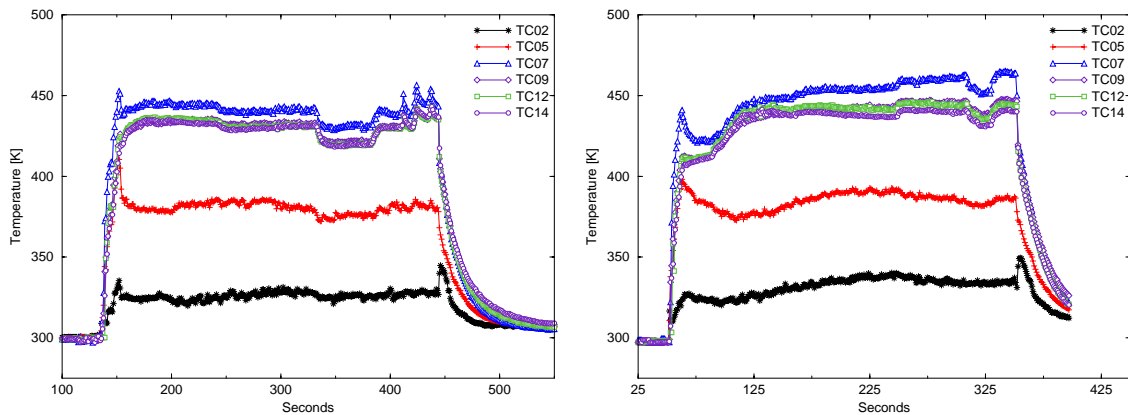

Fig. 22. Temperature versus time for LN_2 injection runs.

2. Water Sheet

After examining the results of the LN_2 injection, it was decided to attempt to overcome the limitations associated with the liquid nitrogen, and shield the IR signature of the nozzle using water. The FLIR camera images in Figure 23 show that a relatively thin sheet of water is capable of completely blocking the IR signature of an object heated to above $772\ K$ ($500\ C$). The left image shows the temperature profile of the carbon steel plate just before initiation of the water sheet. The right image is in the final stages of the test where the water sheet takes a triangular shape. The IR energy radiated by the plate is clearly shielded wherever there is a coherent water

sheet.
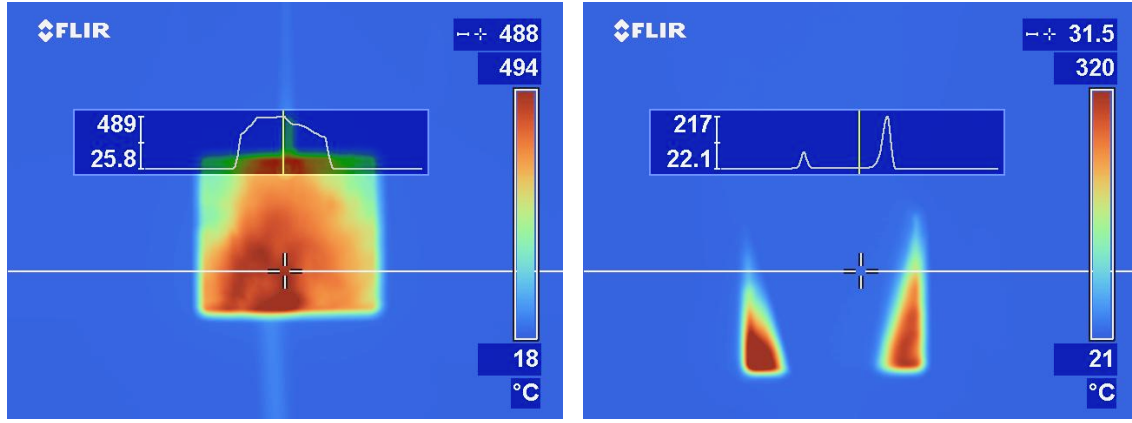
Fig. 23. Temperature profiles of carbon steel plate unshielded (left) and shielded (right).

The experiment was repeated after a thin layer of gold was electroplated onto one half of the plate. Figures 24 and 25 show the four main phases of this test. Phase one -heating the plate; Phase two: -complete shielding with a coherent water sheet; Phase three -as the water level in the reservoir falls, the sheet narrows and whirlpools form causing discontinuities in the sheet; Phase four -the reservoir is almost depleted and only a very narrow water sheet remains.

3.   Water Injection

The encouraging results from the water sheet tests lead to the third and final avenue of the experimental investigation. Water was injected into the exhaust in two ways.
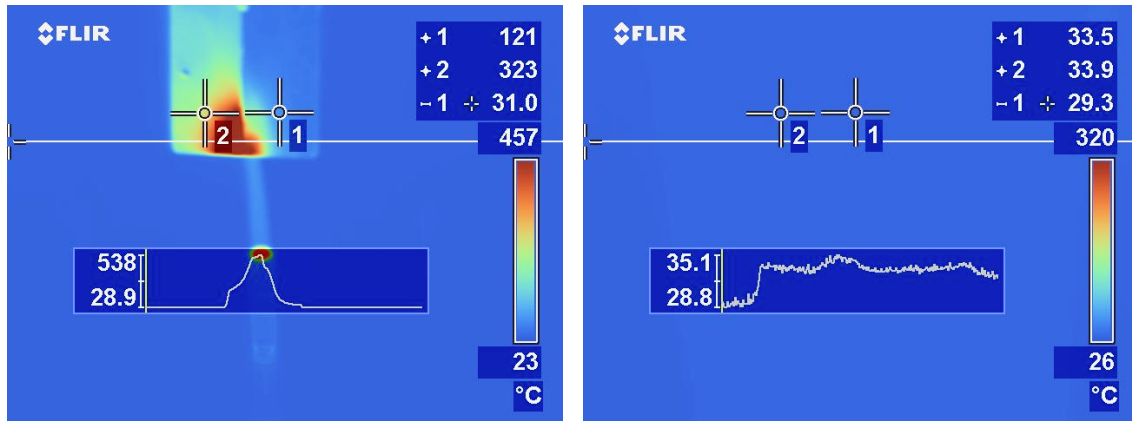
Fig. 24. Thermal images of phases one and two. Phase one: Heating the plate (left) and Phase two: Continuous water sheet (right).

First, water was injected *against* the exhaust jet through a single hole probe. Second, water was injected *with* the exhaust jet through the manifold. In both cases the results were remarkable. Water injection reduced the temperature of the exhaust gases as much as 150 degrees (Fig. 26).

Temperature reductions presented here understate actual reductions by about 47%. Temperatures reported by the FLIR camera are less than physically mesured temperatures because these measurments are taken indirectly via the mirror (Chapter IV Section 4). Measuring the engine temperature through the mirror introduces the emissivity of the mirror which cannot be compensated for by the FLIR camera. This results in the apparent temperature reported by the FLIR camera to be different from the actual temperature. To illustrate, thermocouples in the turbine measure turbine outlet temperature at $861\ K$ ($588\ C$) compared to $552\ K$ ($279\ C$) reported by the FLIR camera. This phenomenon can be minimized by using a highly polished gold mirror instead of the current stainless steel mirror.
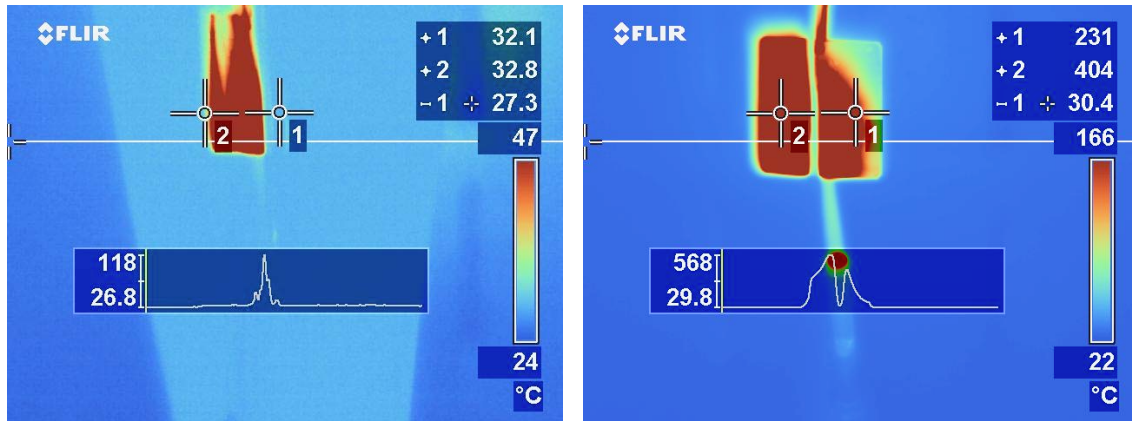
Fig. 25. Thermal images of phases three and four. Phase three: Whirlpools cause discontinuities in water sheet (left) and Phase four: Reservoir depletion narrows water sheet (right).

Although the temperature was dramatically reduced in both injection cases, the probe could not supply the quantity of water necessary to completely shield the IR signature of the engine. Mass flow rate of water through the probe is estimated to be 0.266 kg/s, or about 13.3% of the mass flow of exhaust gasses. The FLIR camera images in Figure 27 show a temperature reduction of only 20 degrees for the hot spot.

On the other hand, the manifold, with an estimated mass flow rate of 2.36 kg/s, or 118% of the mass flow of exhaust gasses, was able supply more than the necessary mass flow of water to completly shield the IR signature of the engine from the FLIR camera. The FLIR camera images in Figures 28 through 30 were recorded sequentially during a one minute water injection sequence. The left image in Figure 29 shows the apparent temperature of the engine before injection and serves as a reference. The right image was recorded seconds after the injection began. Almost immediately the water obscures the engine hot spot. The high temperatures indicated on the left edge of the image are due to the reflection of the exhaust pipe heat by the water cloud.
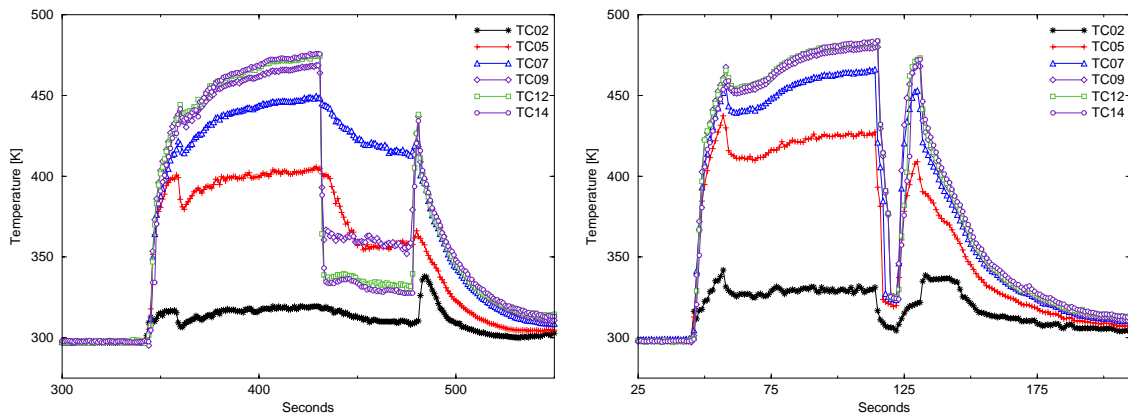
Fig. 26. Temperature versus time for H_2O injection runs.

The temperatures reported by the FLIR camera steadily fall through Figures 29 and 30 reaching a minimum value of 331 K (58 C). During the one minute water injection, the temperature is reduced by 185 degrees. In both injection cases the engine's acoustic signature apparently dropped pitch but the magnitude remained a steady 125 dB in the test cell.
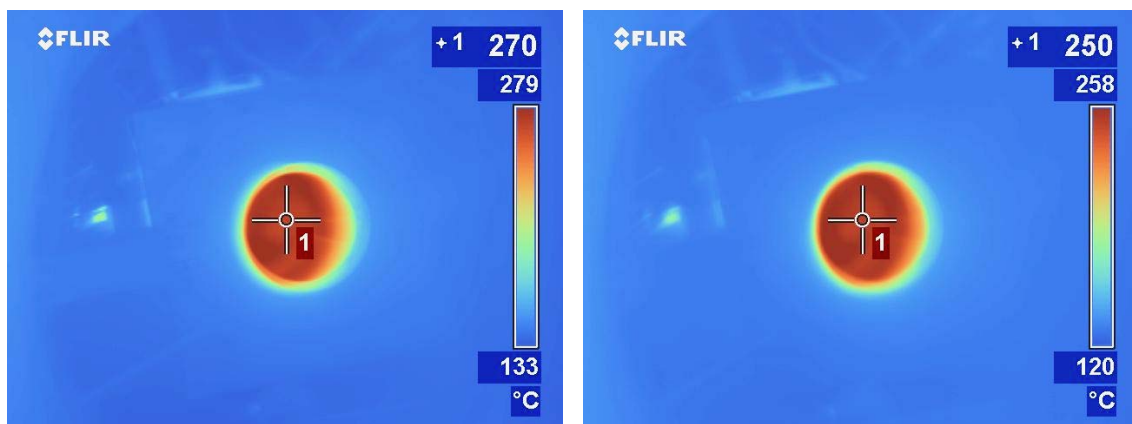

Fig. 27. Aft view thermal image of turbojet before H_2O injection (left) and during injection via probe (right).
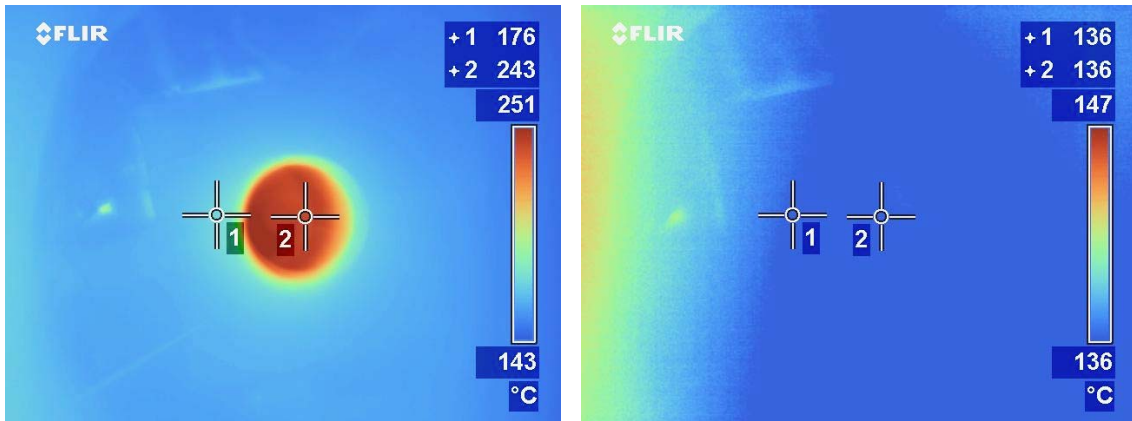
Fig. 28. Aft view thermal image of turbojet before H_2O injection (left) and seconds after injection begins via manifold (right).
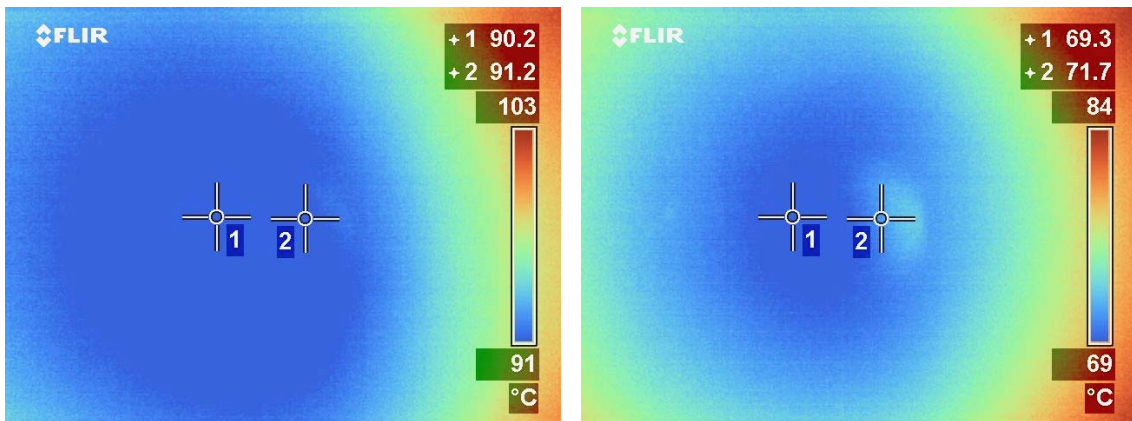
Fig. 29. Aft view thermal image of turbojet during injection via manifold. As injection continues temperatures reported by FLIR camera steadily fall.
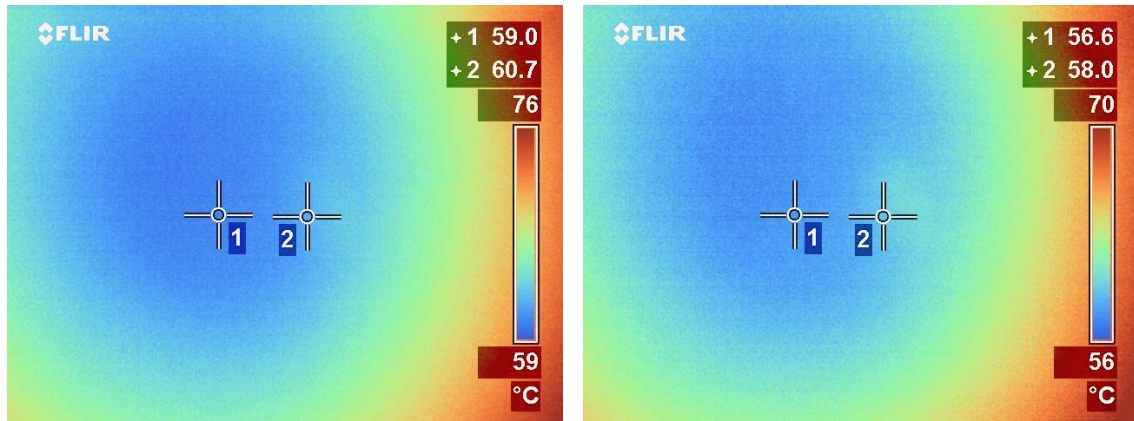
Fig. 30. Aft view thermal image of turbojet during injection via manifold. Tempera-
tures reported by FLIR camera reach a minimum value of 331 K (58 C) for
a total loss of 185 degrees.

43

B.   Numerical Results

The computational part of this research concentrated on verifying thermocouple data collected during the experiments. Two cases ((1) no injection and (2) nitrogen injection at mass flow rate of 1.127 kg/s) were simulated with FLUENT 6.1.22 on two grids with different cell densities. The coarse grid has 16500 cells and the medium grid has 70600 cells.

The temperature contours (Figs. 31 and 32) show the converged results of the coarse grid for the no injection case and the LN_2 injection case respectively. Although difficult to see from these contours, there is an average temperature reduction of approximately 20 degrees in the areas nearest the injector manifold. Beyond TC02 the injected nitrogen is fully mixed and the temperature reduction quickly tapers off. Temperature values for the coarse grid at the second, fifth and seventh TCs are given in Table II.

Fig. 31. Converged results for coarse grid without injection.

Fig. 32. Converged results for coarse grid with $\dot{m} = 1.127 kg/s$ LN_2injection.

The temperature contours shown in Figures 33 and 34 show the converged results

of the medium grid for the no injection case and the LN_2 injection case respectively. For the medium grid, the temperature reduction in the areas nearest the injector manifold was about half of that for the coarse grid. The greatest reduction (approx. 27 degrees) occurs near the fifth thermocouple, beyond which the temperature reduction tapers off as before. Temperature values for the medium grid at the the second, fifth and seventh TCs are given in Table III.

Table II. Coarse grid simulation temperature values at thermocouple locations.

Thermocouple	x	y	T [K] (no inj.)	T [K] (LN_2 inj.)	ΔT
TC02	0.254	0.127	411.788	392.994	-18.794
TC05	0.559	0.127	566.343	558.597	-7.746
TC07	0.864	0.127	604.193	600.270	-3.923

Table IV compares the temperatures from both numerical LN_2 injection cases to thermocouple data collected during experiments. Clearly, the coarse grid simulation grossly overestimates the temperature at all TC locations. Temperatures predicted by the medium grid simulation more closely match measured temperatures and the resolution of a finer grid may improve accuracy.

Figures 35 and 36 present streamtraces on axial velocity contours for the coarse and medium grids respectively. By comparing the streamtrace patterns between the converged solutions, one can determine whether or not the solution is grid independent. The streamtraces in these plots are unmistakably different and therefore the solution remains grid dependent.

Table III. Medium grid simulation temperature values at thermocouple locations.

Thermocouple	x	y	T $[K]$ (no inj.)	T $[K]$ (LN_2 inj.)	ΔT
TC02	0.254	0.127	339.007	328.057	-10.950
TC05	0.559	0.127	515.246	488.316	-26.930
TC07	0.864	0.127	572.060	560.094	-11.966

Table IV. Temperature values (K)at TC locations for LN_2 injection on both grids and two experimental data sets.

Thermocouple	Coarse	Medium	Exp. 3/30	Exp. 4/5
TC02	393	328	325	330
TC05	559	488	375	380
TC07	600	560	435	450

The differences in the temperatures predicted by FLUENT and those recorded during the experiment can be explained by two factors. First, the results from the numerical simulations are steady-state. LN_2 injection is continuous throughout the simulation. In contrast, LN_2 injection is not continuous during the experiment. Once the engine is running at normal operating temperature, LN_2 is injected for five minutes. Second, the simulation does not account for radiant heat lost by the exhaust pipe to the environment. Although ambient temperatures were not recorded during the experiments, the effects of the heat loss are noticeable. After only operating the engine for a short time, the ambient temperature in the test cell is considerably warmer.

The results of the numerical simulations, while not grid independent, do help verify the data collected during the experiment. Most significant is the maximum temperature reduction during injection. The 19 degree drop predicted by the coarse grid confirms the TC data presented in Figure 22.

Fig. 33. Converged results for medium grid without injection.
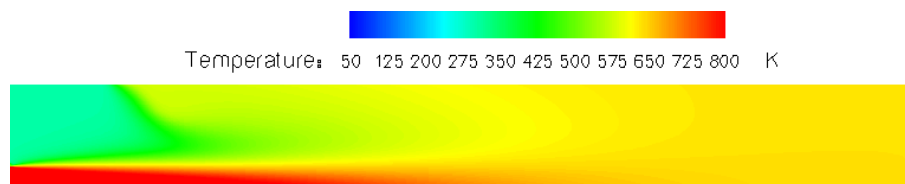
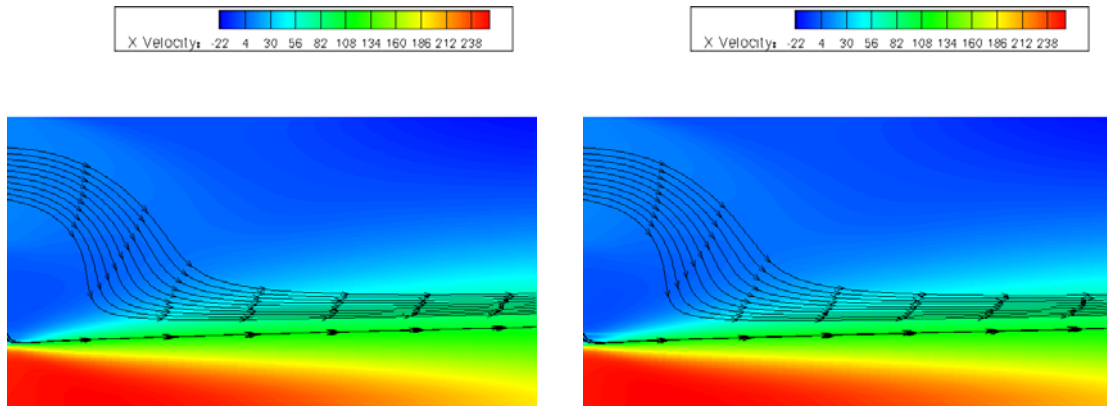Fig. 34. Converged results for medium grid with $\dot{m} = 1.127 kg/s\ LN_2$ injection.

Fig. 35. Streamtraces on x-velocity contour for coarse grid without injection (left and with $\dot{m} = 1.127kg/s$ LN_2 injection (right).
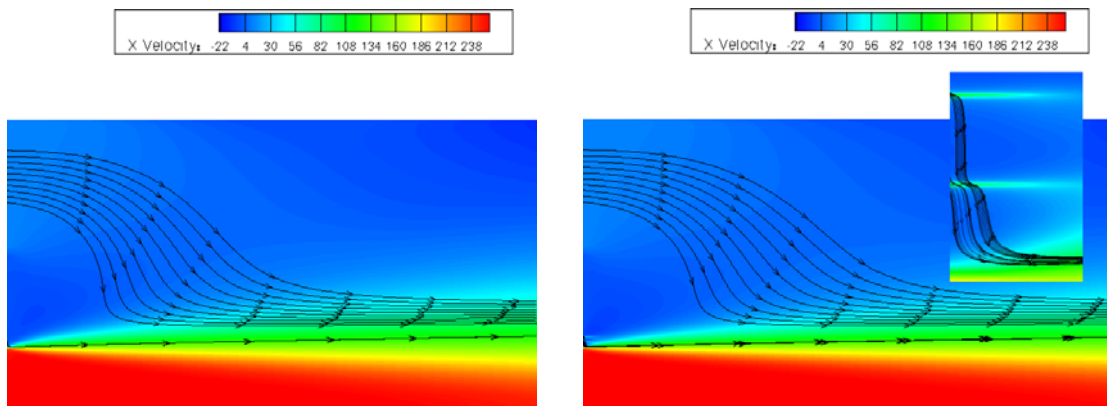
Fig. 36. Streamtraces on x-velocity contour for medium grid without injection (left and with $\dot{m} = 1.127kg/s$ LN_2 injection (right). The insert zooms in at the injector ports.

CHAPTER VI

CONCLUSIONS AND FUTURE WORK

This chapter presents observations concerning the present research. Additionally, it offers recommendations for continued research in the area.

The primary goal of these investigations was to determine the feasibility of reducing the IR signature of a jet engine by injecting liquid nitrogen and water into the exhaust stream. This goal was exceeded. The IR signature of the engine was not only reduced, but completely shielded from detection.

This research, as conducted, illustrates how water may be used to shield the IR signature of hot objects. It is the first work of its kind and lays the foundation for future investigations. Repeatable experiments confirm that a thin coherent sheet of water is capable of completely blocking the IR radiation emitted by a metal plate regardless of the type of metal. Application of this phenomenon was extended to include shielding IR radiation with a water cloud. By injecting a mass flow of water roughly equivalent to the exhaust gas mass flow, the IR signature of the turbojet can be completely shielded. This powerful observation has numerous potential applications including commercial aircraft countermeasure systems.

With many issues left to address, four are of particular interest. First, it is necessary to determine the minimum amount of water necessary to completely shield the engine. Second, determine the thermal imaging effects of electroplating gold onto the exposed surfaces of the nozzle. Third, incorporate thermography into the numerical simulations. The experiments are concerned with the apparent temperature rather than the actual temperature. Currently, the simulations are not comparable to thermal images taken during the experiments. Finally, it seems beneficial to acquire an actual seeker head for detection comparison with the FLIR camera.

REFERENCES

[1] Wallace, J. M. and Hobbs, P. V., *Atmospheric Science; An Introductory Survey*, Academic Press, New York, 1977.

[2] Mahan, J. R., *Radiation Heat Transfer; A Statistical Approach*, John Wiley & Sones, Inc., New York, 2002.

[3] Deyerle, M. C. U., "Advanced Infrared Missile Counter-Countermeasures," *Journal of Electronic Defense*, Vol. 17, No. 1, 1994, pp. 47–50, 67, 70.

[4] Koch, E.-C., "Review on Pyrotechnic Aerial Infrared Decoys," *Propellants, Explosives, Pyrotechnics*, Vol. 26, 2001, pp. 3–11.

[5] Anderson, J. D. J., *Modern Compressible Flow with Historical Perspective*, McGraw Hill, Boston, 2nd ed., 1990.

[6] FLUENT Inc., *FLUENT 6.1.22 User Manual*, Lebanon, NH, January 2003.

[7] Wilcox, D. C., *Turbulence Modeling for CFD*, DCW Industries, Inc., LaCanada, 1998.

APPENDIX A

EXHAUST PIPE WORKING DRAWINGS
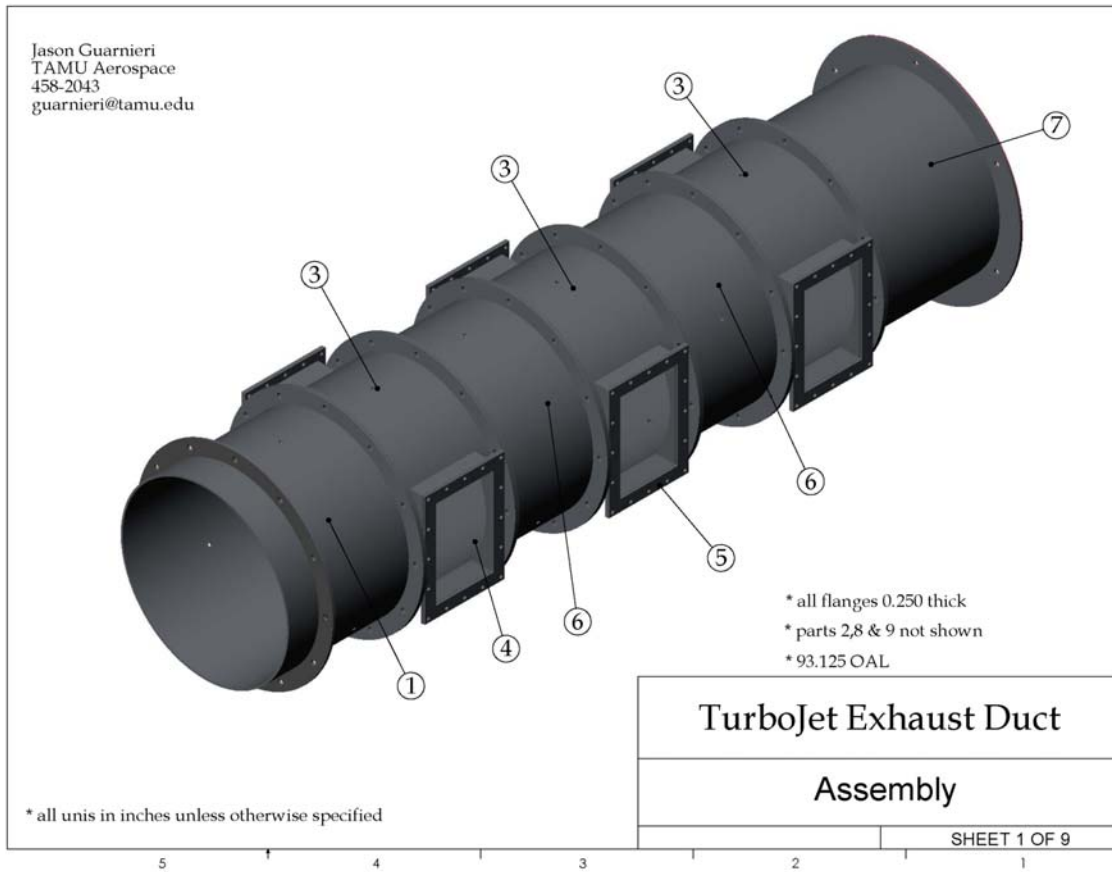
Fig. 37. Exhaust duct assembly.
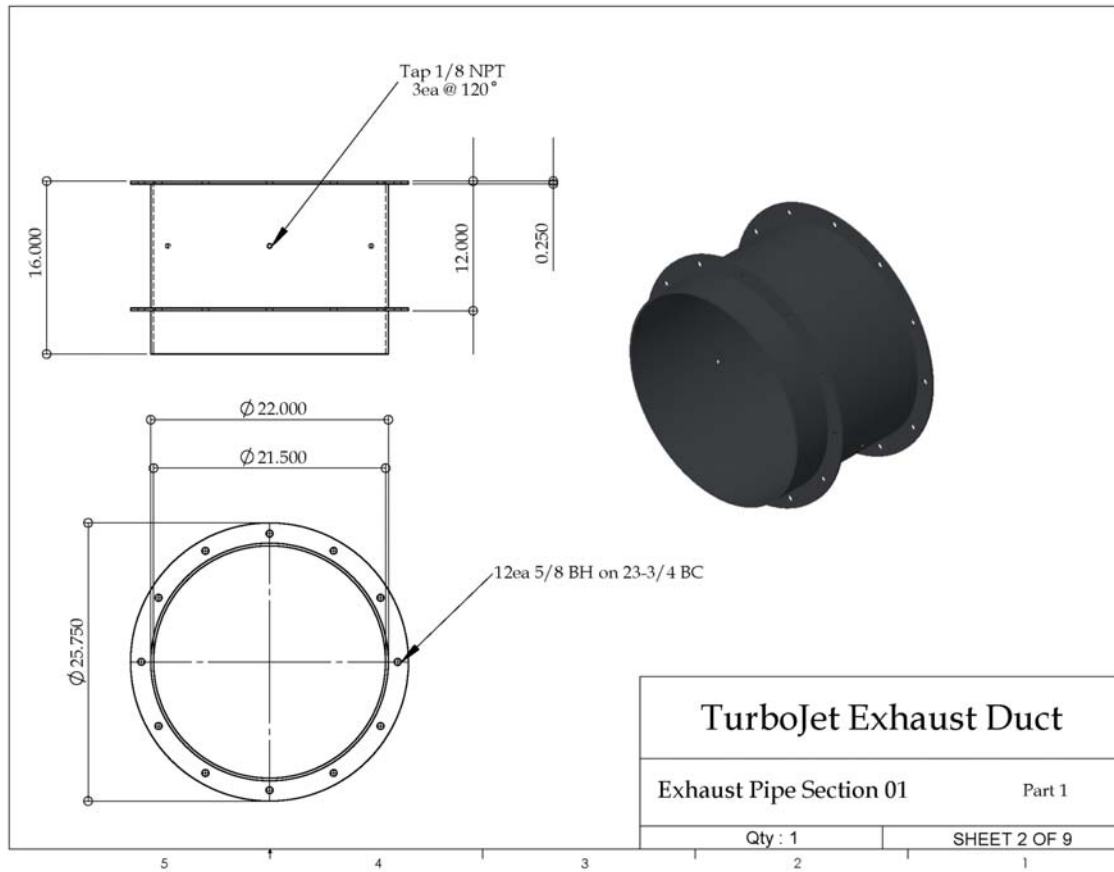
Fig. 38. Exhaust pipe section 01.
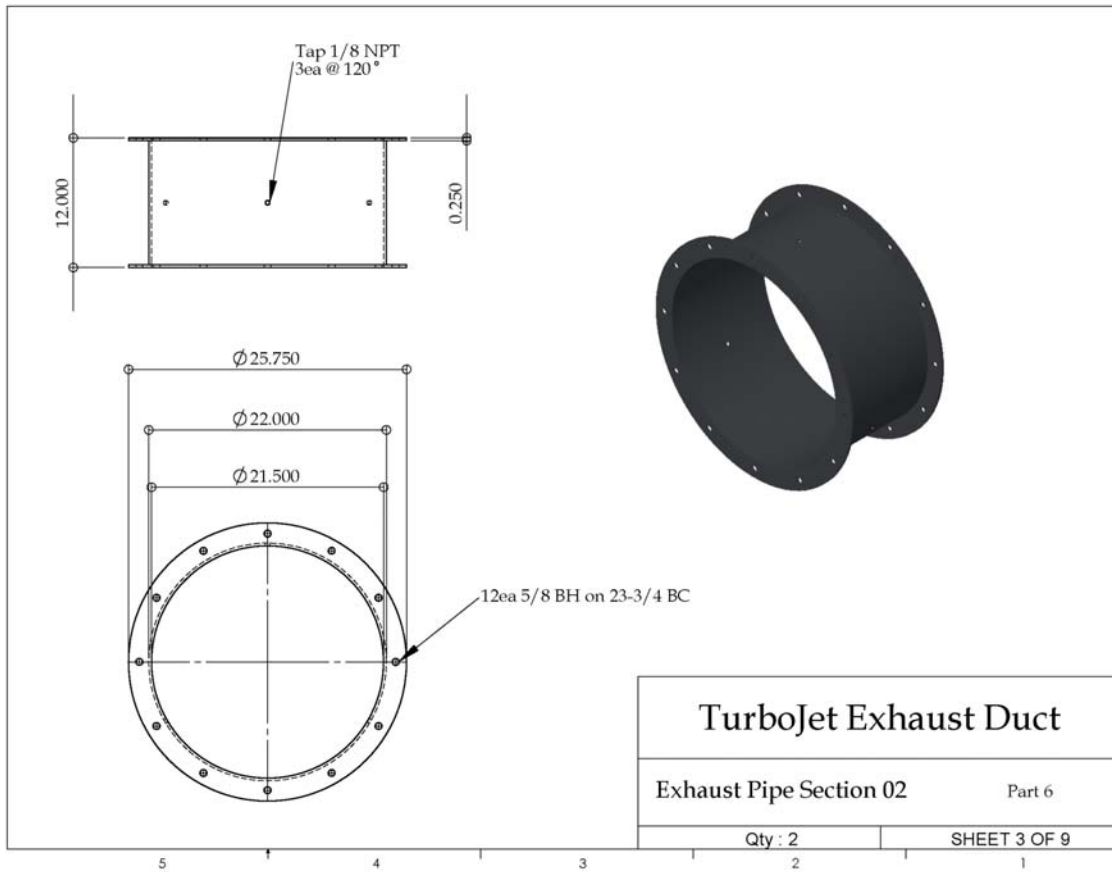
Fig. 39. Exhaust pipe section 02.
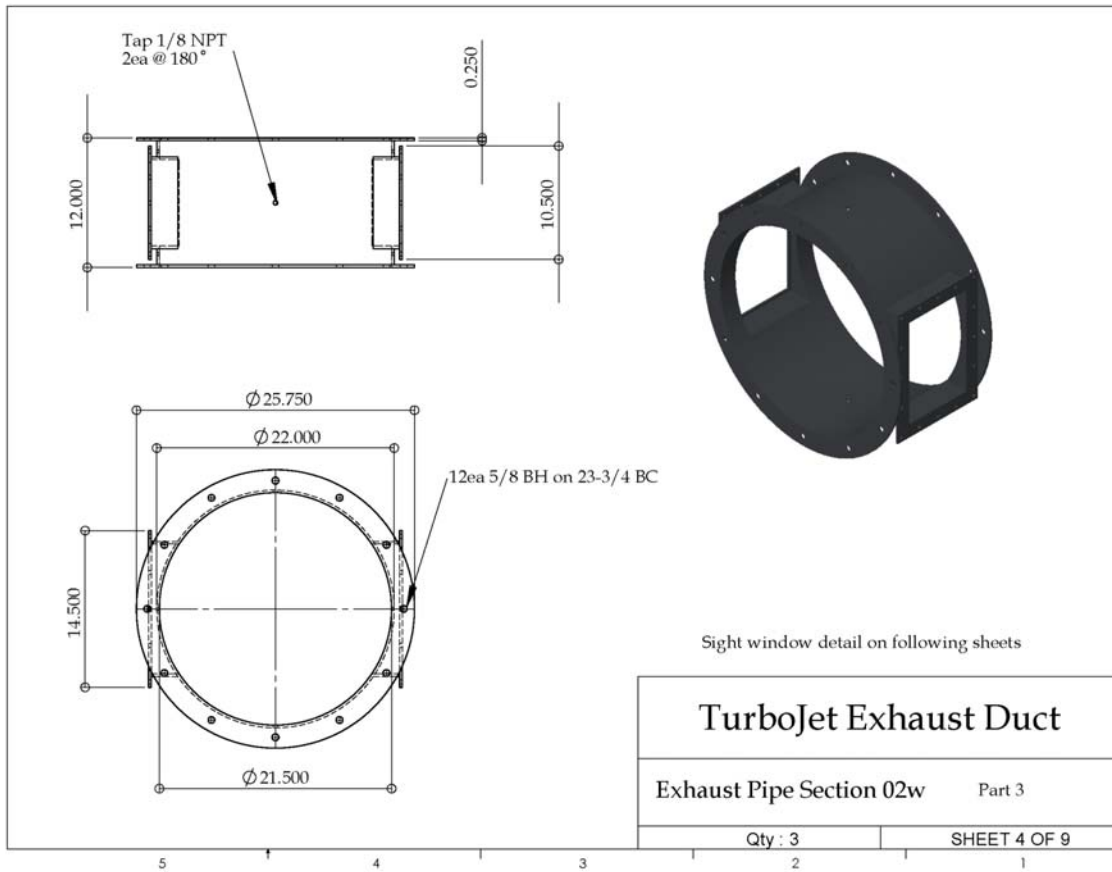
Fig. 40. Exhaust pipe section 02w.
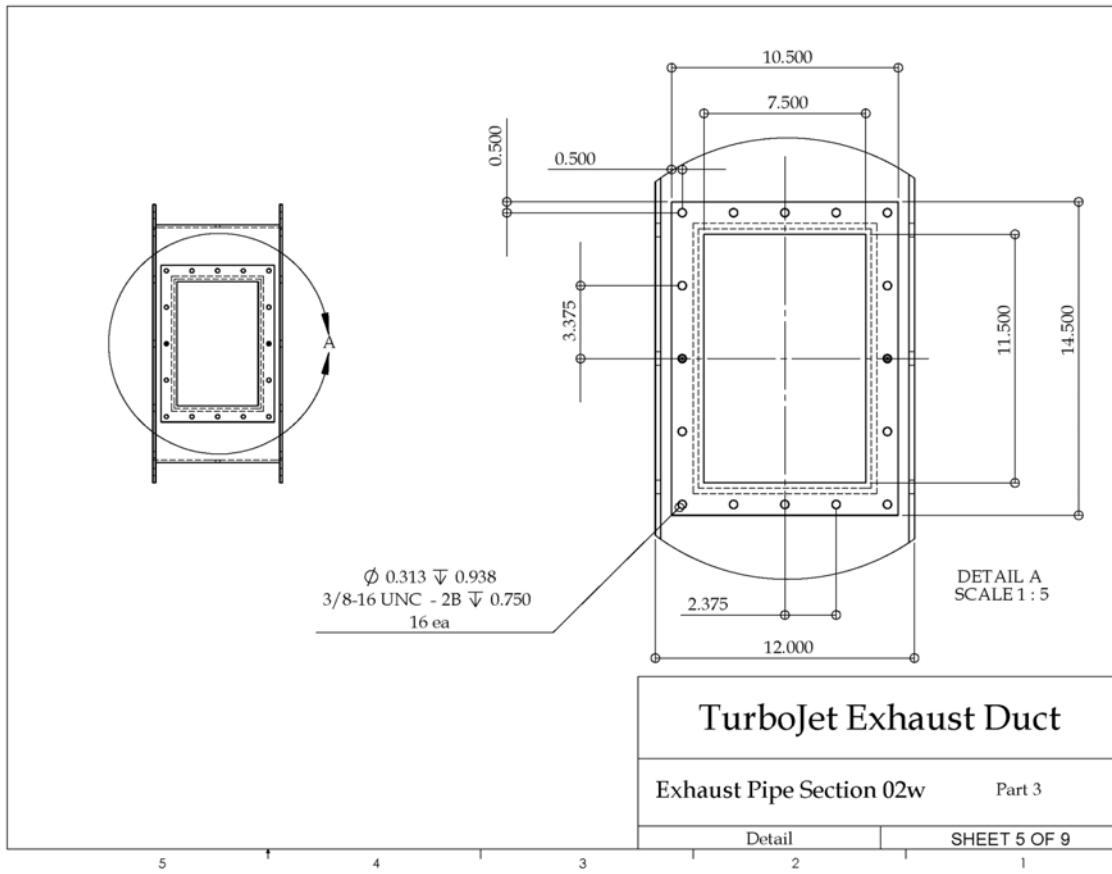
Fig. 41. Exhaust pipe section 02w window detail 1.
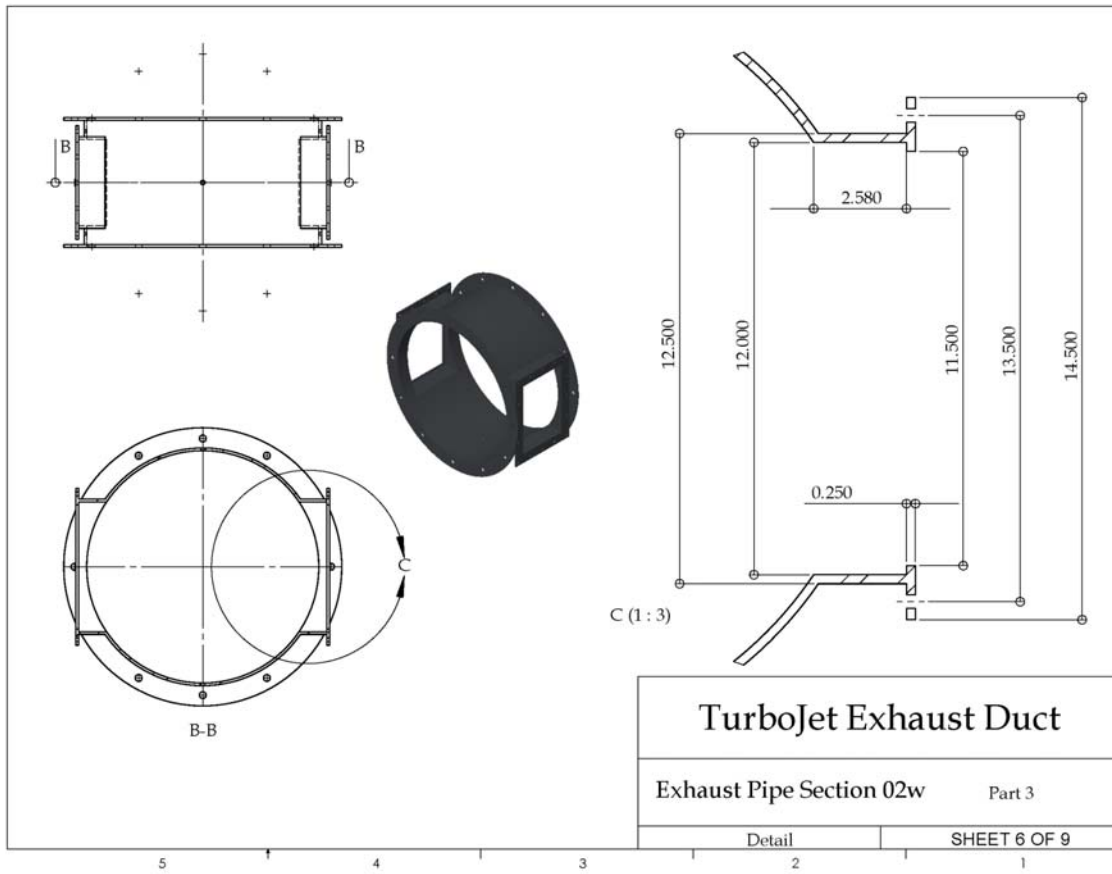
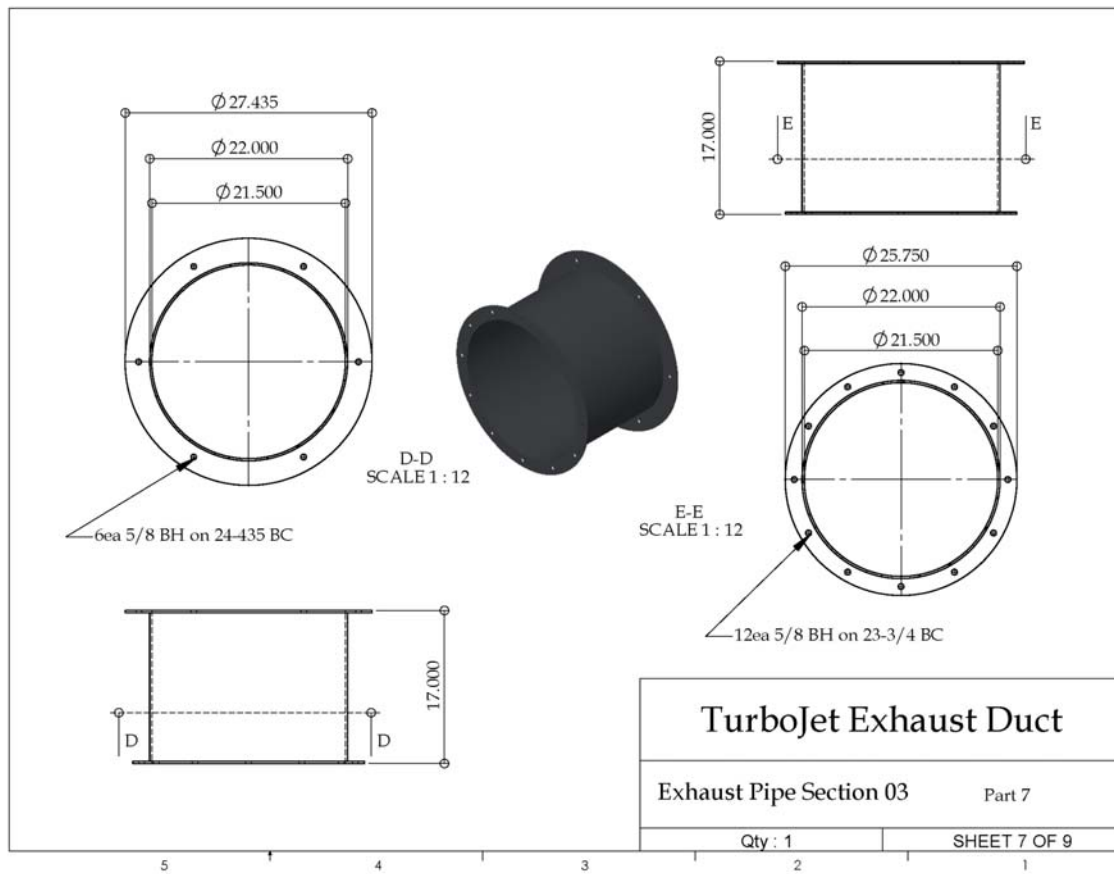Fig. 42. Exhaust pipe section 02w window detail 2.

Fig. 43. Exhaust pipe section 03.

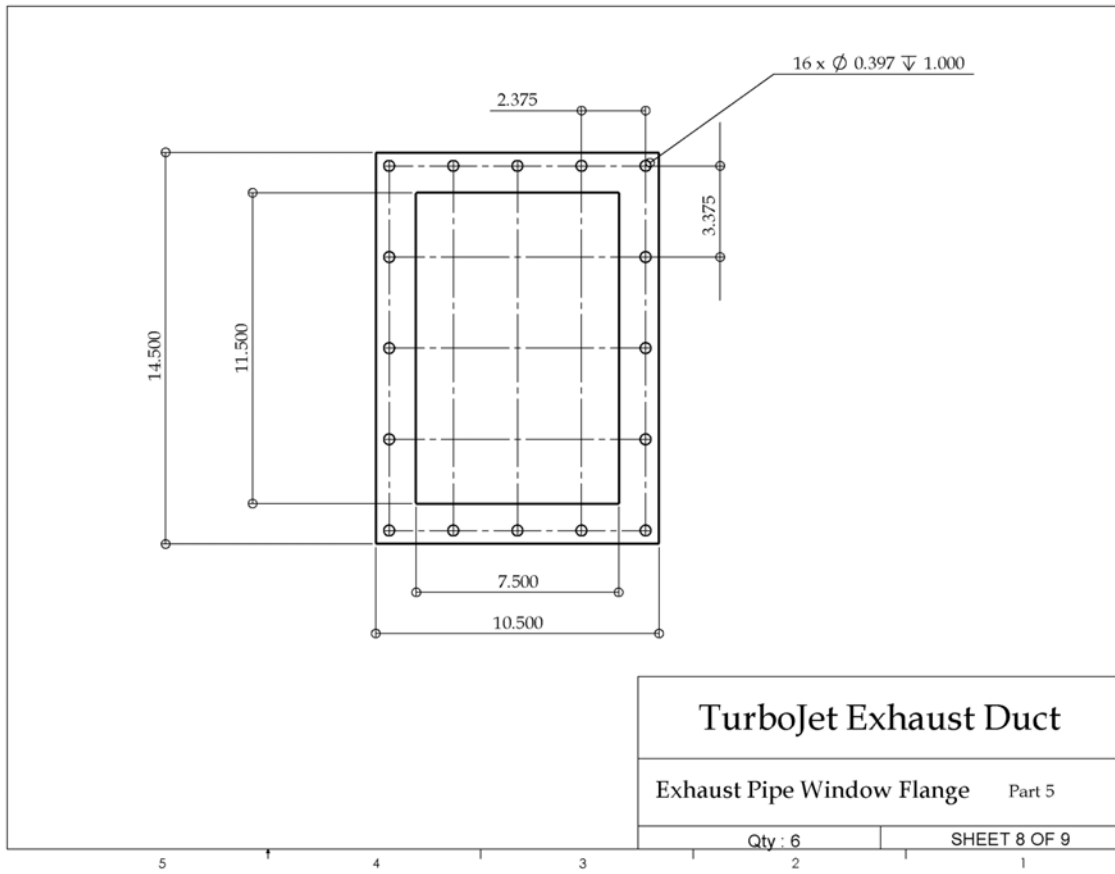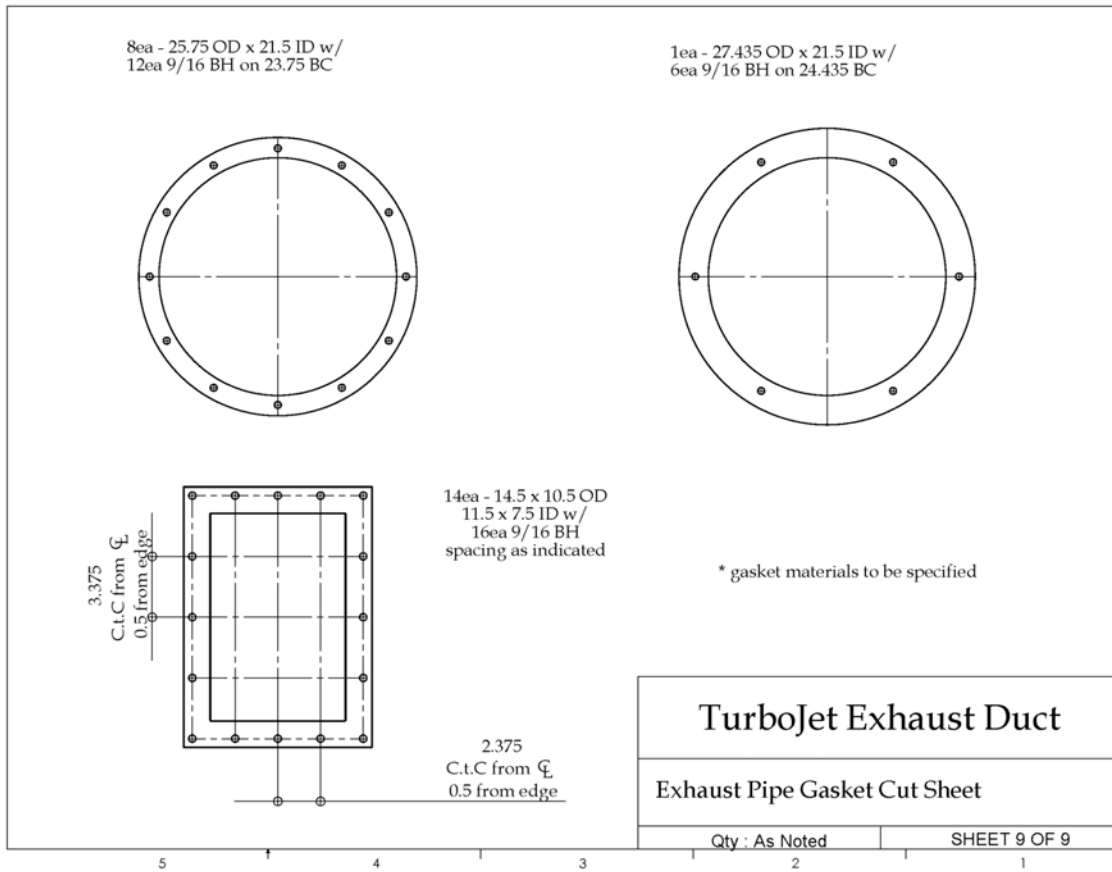Fig. 44. Exhaust pipe window flange.

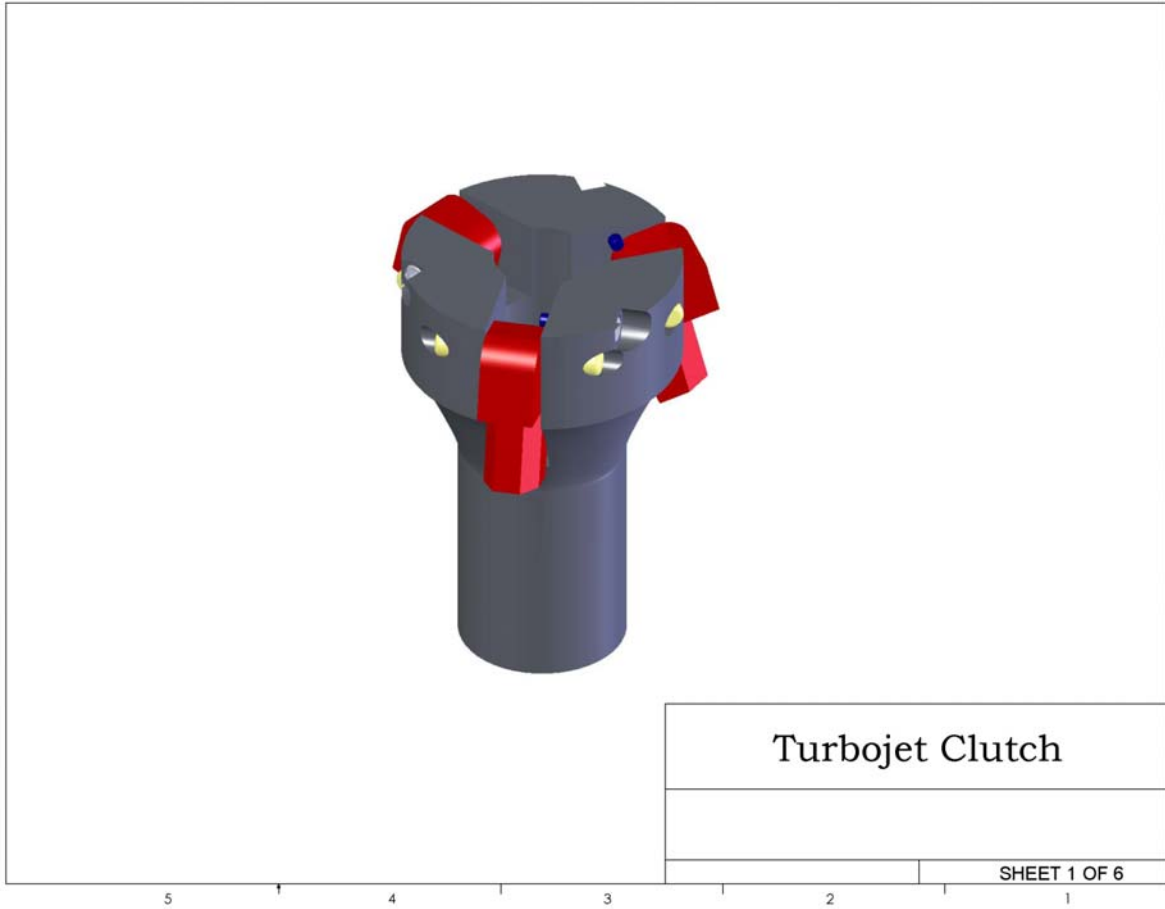Fig. 45. Exhaust pipe gasket cut sheet.
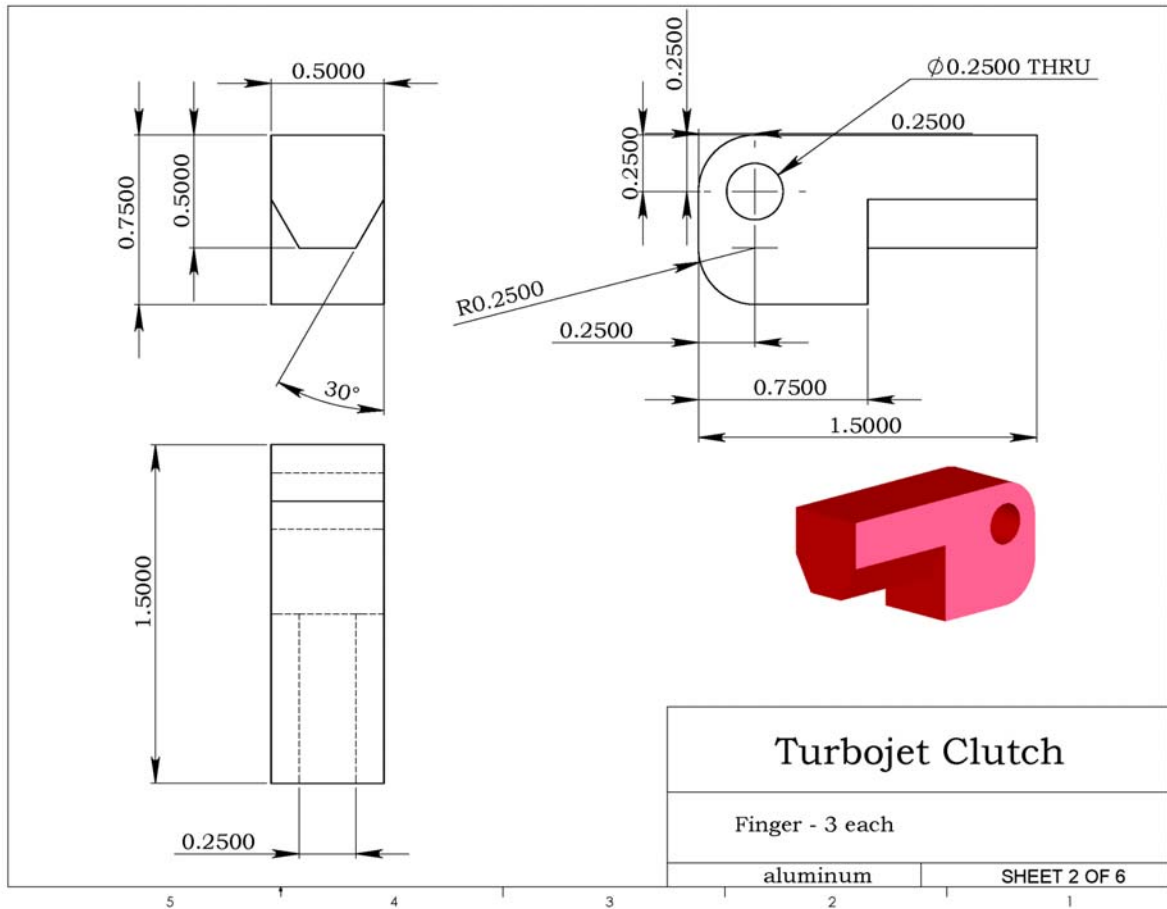
APPENDIX B

CLUTCH WORKING DRAWINGS

Turbojet Clutch

SHEET 1 OF 6

Fig. 46. Clutch assembly.

Fig. 47. Clutch fingers.
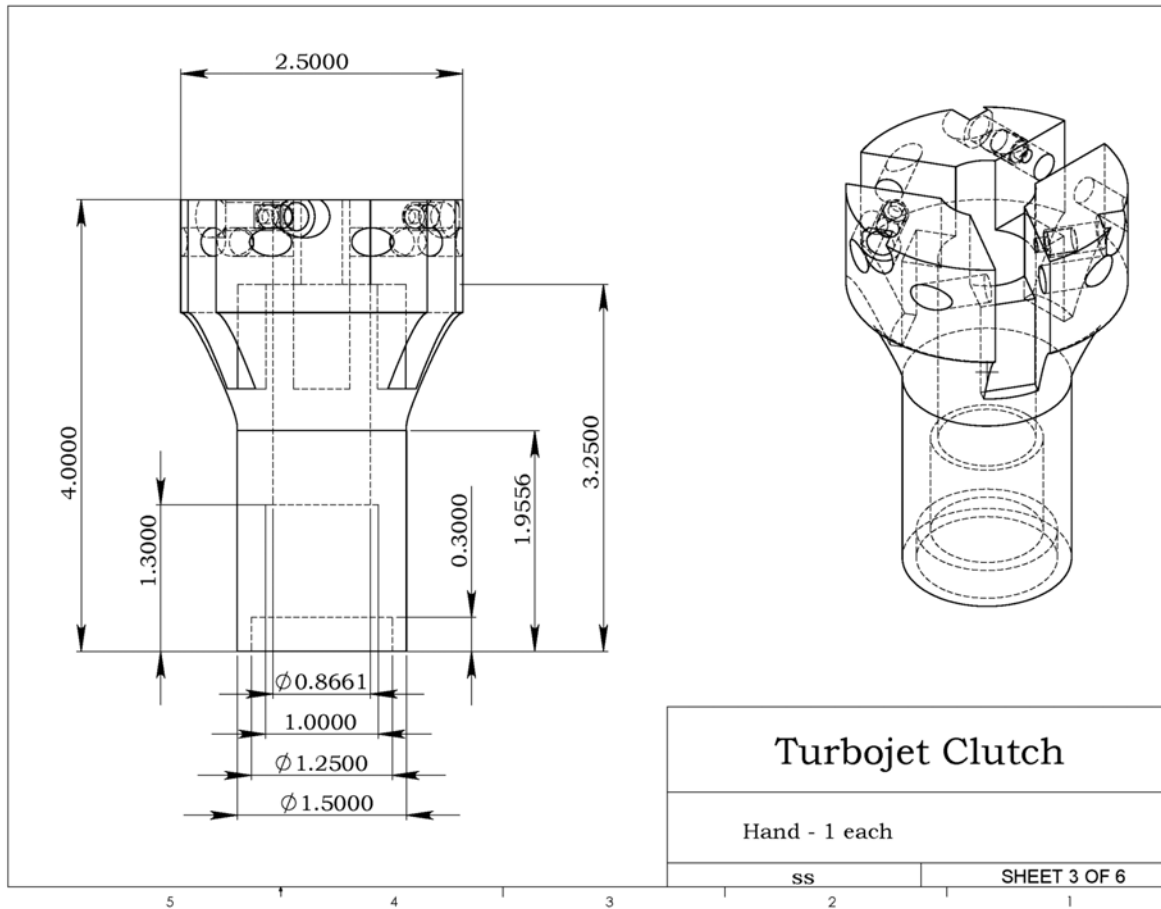
Fig. 48. Clutch main body.

Fig. 49. Clutch main body alternate views.

Fig. 50. Finger arresting pin.
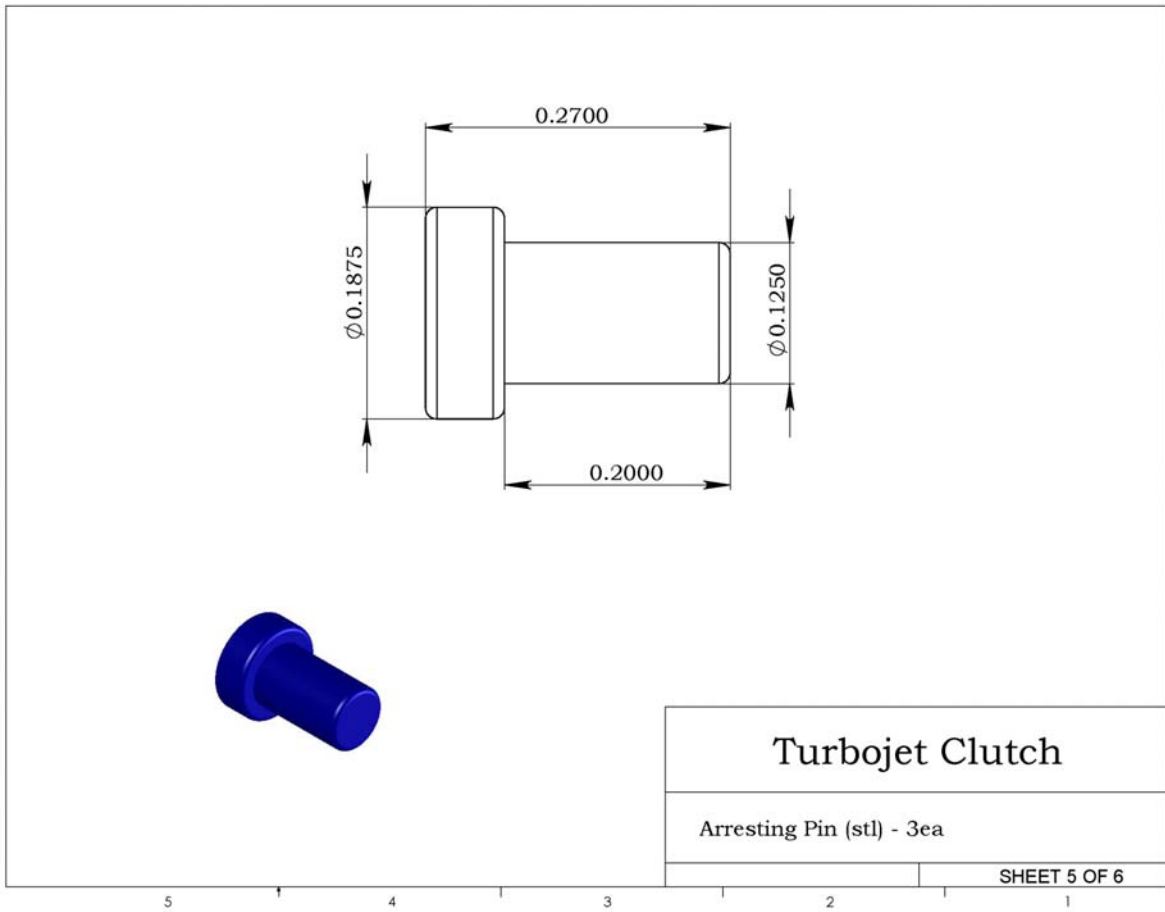
1/4x1-1/2 dowel pin

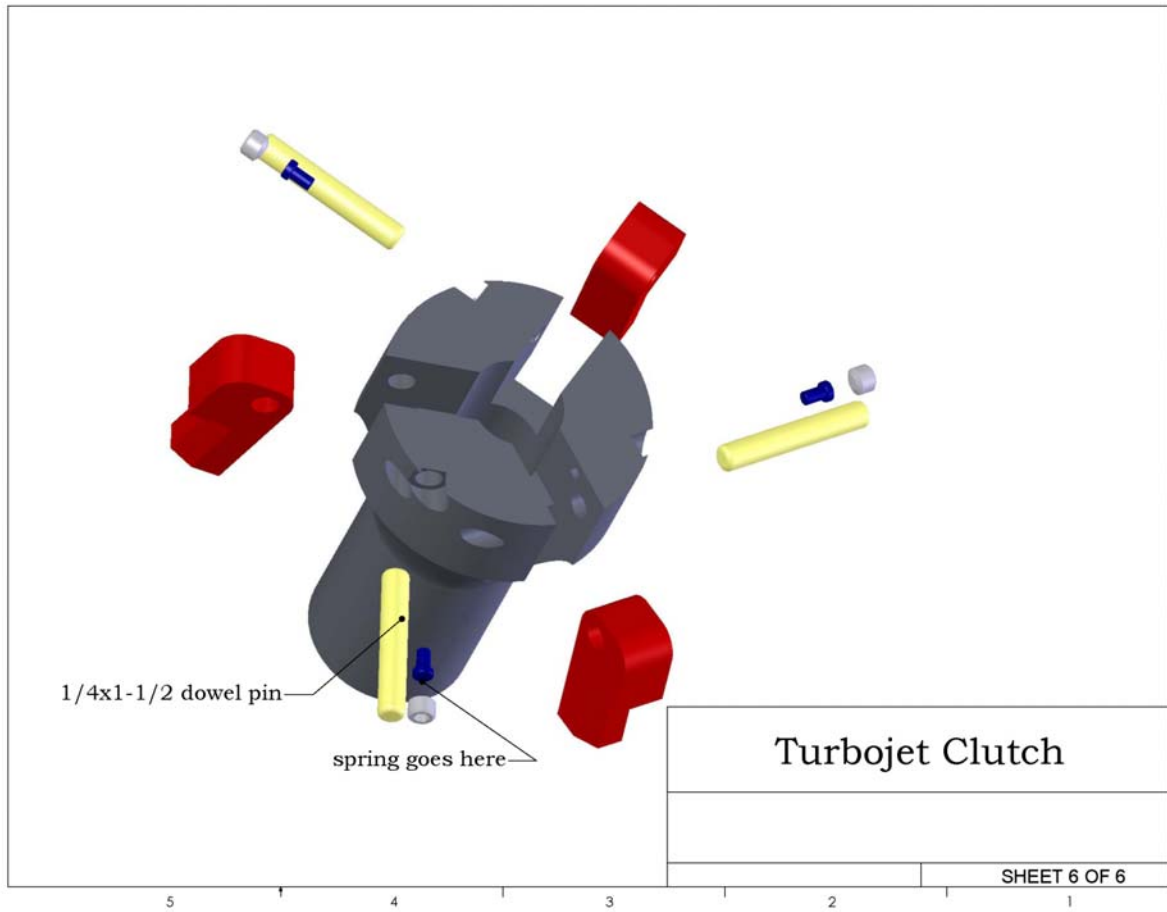spring goes here

Turbojet Clutch

SHEET 6 OF 6

Fig. 51. Clutch exploded view.

VITA

Jason Antonio Guarnieri was born on August 30, 1978 in Beaumont, Texas. He grew up in Beaumont, Texas. He attended Texas A&M University and graduated with a Bachelor of Science in Aerospace Engineering in December 2002.

He entered the graduate program at Texas A&M University the following semester in pursuit of his Master of Science in Aerospace Engineering. His research interests focused primarily on shielding the heat signature of jet engines.

His permanent address is:

325 LittleJohn Dr.

Beaumont, TX 77707-1718